Title

Chaining Superparamagnetic Iron Oxide Nanoparticles and their effect on High-Resolution Magnetic Particle Imaging

Author

Colson, Caylin

Publication Date

2022

Peer reviewed|Thesis/dissertation

Chaining Superparamagnetic Iron Oxide Nanoparticles and their effect on High-Resolution Magnetic Particle Imaging

by

Caylin Colson

A dissertation submitted in partial satisfaction of the

requirements for the degree of

Joint Doctor of Philosophy
with University of California, San Francisco

in

Bioengineering

in the

Graduate Division

of the

University of California, Berkeley

Committee in charge:

Professor Steven Conolly, Chair
Professor Chunlei Liu
Associate Professor Peder Larsen

Summer 2022

Chaining Superparamagnetic Iron Oxide Nanoparticles and their effect on High-Resolution Magnetic Particle Imaging

Abstract

Chaining Superparamagnetic Iron Oxide Nanoparticles and their effect on High-Resolution Magnetic Particle Imaging

by

Caylin Colson

Doctor of Philosophy in Bioengineering

University of California, Berkeley

Professor Steven Conolly, Chair

Magnetic Particle Imaging (MPI) is a noninvasive imaging modality that exploits the saturation properties of superparamagnetic iron oxide particles (SPIOs). A major thrust of MPI research aims to sharpen the magnetic resolution of biocompatible SPIOs, which will be crucial for affordable and safe clinical translation. We recently reported on a new class of MPI tracers —called superferromagnetic iron oxide nanoparticles (SFMIOs) — which offer much sharper magnetic saturation curves. SFMIOs experimentally demonstrate 5-13x improvement in *both* resolution and sensitivity. However, superferromagnetism is a relatively unexplored branch of physics and the nanoscale physics and dynamics of SFMIOs remain a mystery. Here we show experimentally that chaining of SPIOs can explain SFMIO's boost in SNR and resolution. We show how concentration, viscosity, transmit amplitude, and prepolarization time can all affect SPIO chain formation and SFMIO behavior. These experiments will inform strategies on SFMIO chemical synthesis as well as SFMIO data acquisition pulse sequences.

To my mother, who has always had faith in me. In remembrance of my father, the first person who told me I could be an engineer.

Contents

List of Figures

List of Tables

Acknowledgments

First, to Eli, my service dog. Though you can't read this, you have been essential to my PhD journey with your daily support, enforcement of walk breaks, and play. How lucky I am that you like the taste of tears. Thank you for being you and, every day, reminding me to live in the moment.

Thank you to the entirety of the Conolly lab, without whom I couldn't have gotten my PhD! To Steve, thank you for your persistence in training me to analyze problems, starting from their most essential features. From you, I learned that every new thing created must be justified in some way. You cared for me as if I were your family, letting me know that, ultimately, you were looking out for my success. Thank you.

To the other members of the troika, Barry and Quincy, thank you for always listening and for being amazing friends. Barry, your frank feedback and support made getting through the PhD process less lonely. Quincy, your cheerfulness underpinned my whole PhD process and our coffee breaks were a much needed part of my day.

To the other graduate students in the Conolly lab: Xinyi, thank you for your never-ending support and mentorship; I don't know where I'd be in my PhD journey without you. Your candid advice and friendship have been indispensable. Chinmoy, thank you for always listening to and answering my questions, even if they were just nosy and from me reading over your shoulder! Zhi Wei, our overlapping time in the lab was short, but extremely informative. Thank you for being such an inspiration.

To the postdocs in the the Conolly lab: Prashant, thank you for your cheerful can-do attitude; it helped me so much. Ben, thank you for your humor and persistence in reaching research goals. You're the one who really made checking the simplest thing first sink in when debugging (aka make sure the power amplifiers are actually on)! Irati, thank you for inspiring me with your willingness to learn whatever you needed to complete the project. Yao, thank you for your kind words and gentle support when I was faced with problems with my experiments.

To the undergraduates in the Conolly lab: Jacob, thank you for your joyful pursuit of solving problems and pondering results. You've become a good friend throughout your tenure in the lab. Renesmee, thank you for your unremitting work ethic and assistance with all the SFMIO phantom experiments. The both of you have gone above and beyond any expectations one might have had about the role of an undergraduate student in lab. To all the other undergraduates in lab, thank you for your work and support! Your persistence in making nanoparticles has been an essential part of me completing my thesis work.

To Francis: You've been an amazing support to me in the final push of my PhD. You've been a shoulder to cry on, and someone who always builds me up when I'm feeling down. Thank you. I love you!

And finally, to my mother: Thank you for being a never-ending source of support and love. I know I wouldn't have been able to get this far in my life without it. It is difficult to put into words how much your love means to me and how grateful I am for it. I love you.

Chapter 1

Summary of Contributions

1.1 Author Contribution

This dissertation focuses on a dramatic 10- to 20-fold boost in spatial resolution afforded by a breakthrough MPI tracer called superferromagnetic iron oxide nanoparticles, which we will call SFMIOs. This thesis reflects four co-authored papers, a first author manuscript under preparation, and 8 conference abstracts. I start by reviewing MPI and then quickly review prior work to improve spatial resolution in MPI, including Pulsed MPI and larger SPIOs. My specific contribution to the field of MPI is providing the first experimental demonstration that chaining of SPIOs is essential for the nanoscale physics mechanism of SFMIO behavior.

1.2 Publications and Abstracts

This is a list of the publications and abstracts I have co-authored during my PhD.

1.2.0.1 Publications

1. Prashant Chandrasekharan et al. "A perspective on a rapid and radiation-free tracer imaging modality, magnetic particle imaging, with promise for clinical translation". In: *The British Journal of Radiology* 91.1091 (2018). p. 20180326. doi: 10.1259/bjr.20180326.

2. Prashant Chandrasekharan et al. "Using magnetic particle imaging systems to localize and guide magnetic hyperthermia treatment: tracers, hardware, and future medical applications". In: *Theranostics* 10 (2020). pp. 2965–2981. doi: 10.7150/thno.40858.

3. Yao Lu et al. "Combining magnetic particle imaging and magnetic fluid hyperthermia for localized and image-guided treatment". In: *International Journal of Hyperthermia* 37.3 (2020). pp. 141–154. doi: 10.1080/02656736.2020.1853252.

4. Prashant Chandrasekharan et al. "Non-radioactive and sensitive tracking of neutrophils towards inflammation using antibody functionalized magnetic particle imaging tracers". In: *Nanotheranostics* 5.2 (2021). pp. 240–255. doi: 10.7150/ntno.50721.

5. Zhi Wei Tay et al. "Superferromagnetic Nanoparticles Enable Order-of-Magnitude Resolution & Sensitivity Gain in Magnetic Particle Imaging". In: Small Methods 5.11 (2021). p. 2100796. doi: 10.1002 /smtd.202100796.

6. Caylin Colson et al. "Evidence that SPIO Chain Formation is Essential for High-Resolution MPI." In: *IEEE Transactions of Medical Imaging*. (2022). In preparation.

1.2.0.2 Conference Abstracts

1. Prashant Chandrasekharan, et al. "Immune Cell Tracking with Magnetic Particle Imaging". Poster presented at World Molecular Imaging Conference, Seattle, WA. 2018.

2. Caylin Colson, et al. "Evidence that SPIO Chain Formation is Essential for Super-Resolution MPI". Poster presented at World Molecular Imaging Conference, Montreal, Canada. 2019.

3. King Long Barry Fung, et al. "Dynamics of chain formation and decay for super-resolution Magnetic Particle Imaging". Poster presented at World Molecular Imaging Conference, Montreal, Canada. 2019.

4. Zhi Wei Tay, et al. "Order-of-Magnitude Resolution and SNR improvement using Positive Feedback MNP chains in Magnetic Particle Imaging". Presentation at World Molecular Imaging Conference, Montreal, Canada. 2019.

5. Prashant Chandrasekharan, et al. "Surface protein targeted molecular imaging approach for tracking white blood cells to inflammation using Magnetic Particle Imaging". Poster presented at World Molecular Imaging Conference, Montreal, Canada. 2019.

6. Caylin Colson, et al. "Evidence that SPIO Chain Formation is Essential for Super-Resolution MPI". Presentation at Northern California Chapter of the American Association of Physicists in Medicine, Young Investigator's Symposium, Online. 2020.

7. Caylin Colson, et al. "Evidence that SPIO Chain Formation is Essential for Super-Resolution MPI". Presentation at MPI Rising Stars E-Symposium, Online. 2020.

8. Caylin Colson, et al. "Measuring SPIO Chain Formation Times for Super-Resolution MPI with Magnetic Particle Relaxometry". Poster presented at World Molecular Imaging Conference, Online. 2020.

9. King Long Barry Fung, et al. "Surface protein targeted white blood cell tracking of inflammation using Magnetic Particle Imaging (WBC-MPI)". Presentation at World Molecular Imaging Conference, Online. 2020.

10. Prashant Chandrasekharan, et al. "Monitoring outcome of hyperthermia treatment by measuring relaxation induced blurring with magnetic particle spectroscopy". Poster at World Molecular Imaging Conference, Online. 2020.

11. Quincy Huynh, et al. "Employing Active and Passive Compensation to Improve SNR of Arbitrary Waveform Relaxometer." Poster at World Molecular Imaging Conference, Online. 2020.

12. Caylin Colson, et al. "Measuring Chain Formation Times for Super-Resolution MPI with Magnetic Particle Relaxometry". Presentation at Northern California Chapter of the American Association of Physicists in Medicine, Young Investigator's Symposium, Online. 2021.

13. Caylin Colson, et al. "Chain Formation is Essential for Super Resolution MPI". Presentation at World Molecular Imaging Conference, Online. 2021.

14. King Long Barry Fung, et al. "Non-radioactive and sensitive tracking of neutrophils and macrophages towards inflammation using antibody functionalized magnetic particle imaging tracers". Presentation at World Molecular Imaging Conference, Online. 2021.

15. Quincy Huynh, et al. "Optimized Coil Design for Direct Feedthrough Suppression in Magnetic Particle Imaging". Poster presented at World Molecular Imaging Conference, Online. 2021.

16. Chinmoy Saayuja, et al. "Computational modeling of superferromagnetism in finite-length chains of Superparamagnetic Iron Oxide tracers for use in super-resolution Magnetic Particle Imaging". Poster presented at World Molecular Imaging Conference, Online. 2021.

17. Caylin Colson, et al. "Measuring Chain Formation Times for Super-Resolution MPI with Magnetic Particle Relaxometry". Presentation at MPI Rising Stars E-Symposium, Online. 2021.

18. Caylin Colson, et al. "Chain Formation is Essential for Super Resolution MPI". Presentation at 37th Annual Bioengineering Conference and Retreat, Online. 2021.

19. King Long Barry Fung, et al. "Elucidating super-resolution Magnetic Particle Imaging superferromagnetic remanence decay through MPI signal evolution informs super-resolution MPI scan strategies". Presentation at International Workshop on Magnetic Particle Imaging, Online. 2022.

Chapter 2

Introduction to Magnetic Particle Imaging

2.1 Overview of Magnetic Particle Imaging and its applications

In this section, I will discuss the general strengths of Magnetic Particle Imaging. I will then go over the applications of MPI in the field of medical imaging and the first *in vivo* proof of concept experiments that have been demonstrated.

2.1.1 MPI: A unique medical imaging modality

Magnetic Particle Imaging (MPI) is a radiation-free, non-invasive medical imaging modality developed in 2005 by Gleich and Weizenecker [1]. MPI is a tracer imaging modality, similar to other modalities like nuclear medicine. A tracer imaging modality is, generally, a process where a contrast agent is injected, produces a signal, and is then imaged throughout the body. Tracer imaging methods either highlight blood vessels (angiography), pathophysiologic biomarkers, like the high metabolic rate of tumors (FDG PET), infection imaging (^{111}In-WBC), and pulmonary embolism imaging (MAA-^{99m}Tc Scintigraphy/SPECT. MPI could soon offer a radiation-free complement to all of these Nuclear Medicine studies.

MPI images the magnetization of superparamagnetic iron oxide nanoparticles (SPIOs). This generates an image that shows the location and concentration of SPIOs within the body. MPI's strengths compare to other imaging modalities in the following ways:

- *No attenuation:* MPI signal strength does not change as a function of its depth within tissue. There is low attenuation of electromagnetic fields below 100 MHz; MPI uses very low frequency (20 kHz–20 MHz) magnetic fields [2]. Depth attenuation is a challenge for many imaging methods, including optical, ultrasound, and SPECT and sometimes artifacts can render the attenuation-corrected scans unreliable. [3].

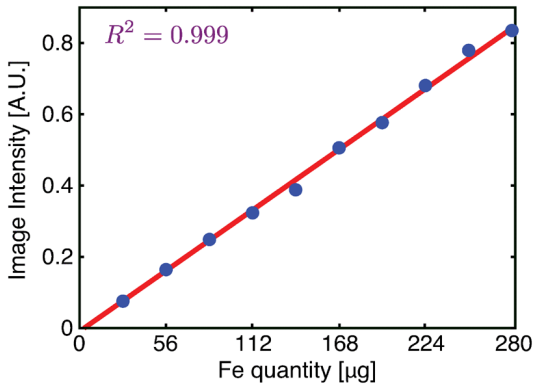

Figure 2.1: Experimental demonstration of MPI's quantitation: MPI signal strength is linear with the amount of iron in a voxel, showing a near perfect correlation constant of $R^2 = 0.999$. ©2013 IEEE. Reprinted with permission from [4].

- *Linear and Quantitative:* Unlike previously mentioned modalities, MPI images are linear and quantitative. The strength of the signal in each voxel is perfectly linear to the amount of iron within a voxel [4–6]. The SPIO magnetization imaged is a sum of the individual magnetic moments of each nanoparticle. Fig. 2.1 shows the quantitative nature of MPI by comparing the iron content of a voxel versus its MPI signal. This demonstrates the linear relationship between the MPI signal and the amount of iron in a voxel.

- *Positive Contrast:* SPIOs are sometimes employed as T2* contrast agents in MRI. However, the signal created is a signal loss in the image, not positive contrast [3, 7]. MPI signals have positive contrast because MPI only images the nonlinear magnetization of SPIOs [1]. MPI has superb contrast-to-noise ratio (CNR) because there is zero signal from surrounding mammalian tissue.

- *Highly Sensitive:* MPI scans are decidedly sensitive, with measurements down to nanograms of iron per voxel [5, 6]. The magnetic moment of SPIOs is much higher than other magnetic materials. Compared to the sensitivity of MRI, MPI is much more sensitive because the electronic magnetization of SPIOs is 22 million times greater than the nuclear magnetization of ^{1}H in MRI at 7T [8]. MPI's dose-limited sensitivity is well suited to imaging even micromolar tracer concentrations [8] whereas MRI SNR is limited to 100 mM tracer concentrations (e.g., 19F). Of course, MRI anatomical enjoys endogenous water concentration of 55M so this MRI sensitivity challenge is only a problem for imaging tracers.

- *Non-radioactive, safe, tracer:* MPI uses SPIOs as tracers that are non-radioactive and safe for human use. One SPIO, Feraheme (ferumoxytol), is approved for clinical

usage for the treatment of iron-deficient anemia in patients with chronic kidney disease (CKD) [9]. Clinical ferumoxytol treatment in the US generally consists of two doses of 510 mg with a concentration of 30 mg Fe/ml [10]. Considering the sensitivity of this modality, MPI's use of iron oxide tracers is well within the safe dosage range. This ferumoxytol steady state concentration is about 0.5 mM, which is much higher than the 1 micromolar sensitivity threshold.

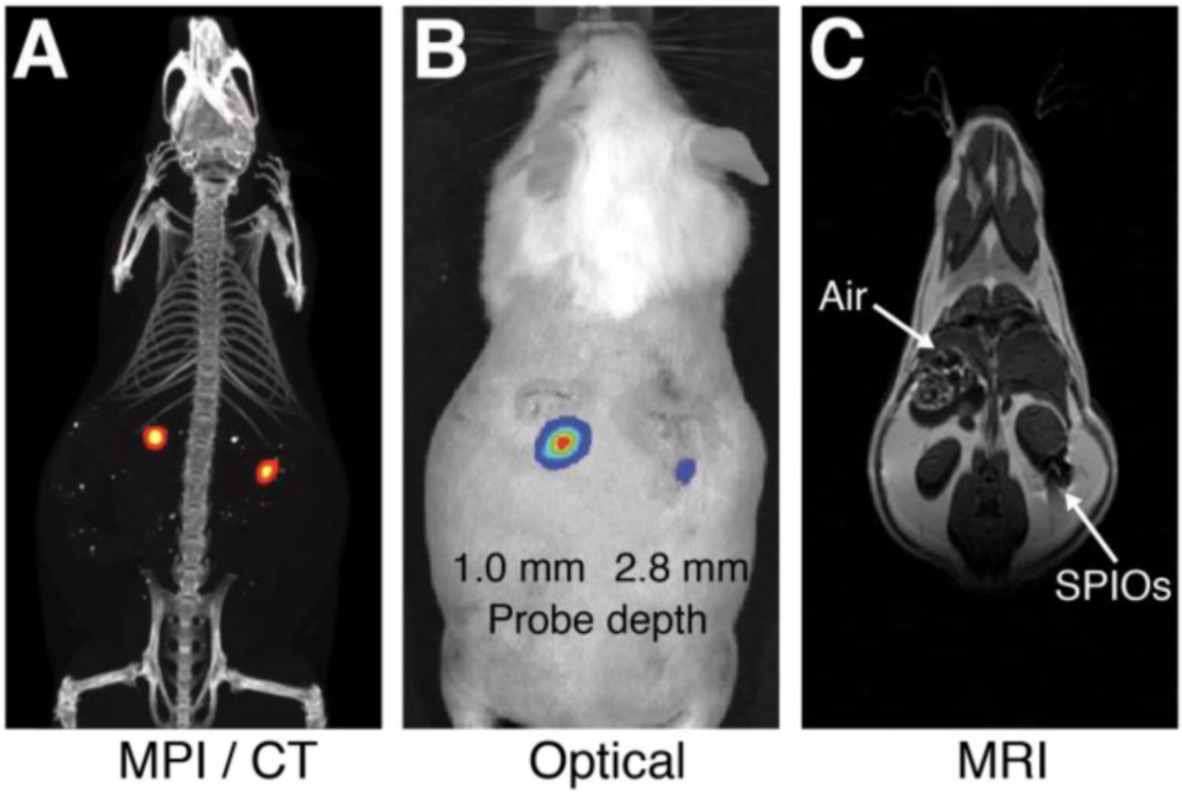

Figure 2.2: MPI/CT, MRI, and Optical Imaging Comparison. In this image, two point sources composed of a mixture of SPIOs and fluorescent tracer (Nanomag-MIP and Angiosense 680 EX, respectively) were implanted at two different depths below the dorsal skin surface of a mouse. (a) MPI/CT image shows no depth attenuation through tissue. MPI Scan characteristics: 5 x 3.75 x 10 cm FOV, 6.8 min scan. CT scan characteristics, 15 min scan, 184 μm isotropic resolution. (b) Optical imaging (fluorescence) shows signal attenuation as function of probe depth. 5 second scan. (c) MRI images show loss of signal in tissue image, much like the xair pockets seen. MRI scan characteristics: 4 x 8 cm FOV, 313 μm in-plane resolution, 17 min scan. Republished with permission of Theranostics, [6]; permission conveyed through Copyright Clearance Center, Inc.

Fig. 2.2 shows a comparison between MPI, optical, and MRI modalities when imaging bioluminescent-labeled SPIOs. In Fig. 2.2 (a) and (b), two identical tracers were placed 1 mm and 2.8 mm deep within a mouse torso. In Fig. 2.2 (b) we see an example of the signal dependence on depth attenuation that plagues optical images. Though the amount of tracer is identical between the two probes, the probe that is 2.8x deeper into the mouse torso shows a significant drop in signal strength. The MPI image in Fig. 2.2 (a), however, shows no change in signal as a function of depth within the torso. Fig. 2.2 (a) and (c) shows how SPIO use in MRI compares with SPIO signals in MPI. In Fig. 2.2 (c), SPIOs are shown as a loss of signal, where the SPIO scrambles the MRI phase of the ^{1}H surrounding it. The loss of signal shows in an image the same way an air pocket does, where there is no ^{1}H at all. Specialized positive contrast SPIO pulse sequences have been developed [11], but the MRI image shows the background tissue that surrounds the SPIOs, not the SPIOs themselves. This is not the case in 2.2 (a) where no background tissue is seen at all in the MPI scan. MPI only images the signal of the tracer, which creates positive contrast.

2.1.2 MPI applications

MPI is a tracer imaging modality with applications in cancer imaging, cell tracking, vascular imaging, and magnetic fluid hyperthermia. The strengths of MPI are its sensitivity, high contrast, zero depth attenuation, infinite persistence, robustness, and zero radiation. These strengths lend themselves well to the applications in the following section.

2.1.2.1 Cancer Imaging in MPI

Magnetic Particle Imaging has been shown to be an effective way to visualize tumors by taking advantage of the enhanced permeability and retention effect (EPR). The EPR effect describes how the "neovasculature" created to feed a tumor is "leaky", lacking the tight junctions of healthy vasculature. Nanoparticles and macromolecules tend leak out of blood circulation within a tumor and remain near the tumor for hours [14–16].

Yu et al. [12] showed that the EPR effect could be used to visualize xenografted breast tumors with MPI following a tail vein injection of SPIO tracers. The work showed an initial wash-in rim enhancement that highlighted the position of the tumor. By 6 hours post injection, a tumor-to-background ratio of 50 was seen, demonstrating MPI's capabilities for high contrast imaging.

Nanoparticles can also highlight cancer if a targeting ligand (e.g., peptides or antibodies) can bind the circulating SPIO to targets very close to the tumor. MPI has also visualized tumors using active targeting of nanoparticles to tumors. Arami et al. used lactoferrin-assisted accumulation of nanoparticles to a xenografted glioma model placed on the right flank of a mouse [13]. This was then imaged within 2 hours post IV injection. In Fig. 2.3 (b), a permanent magnet was placed on the right side flank to increase nanoparticle loading in the tumor. However, even without the permanent magnet, the tumor was still highlighted

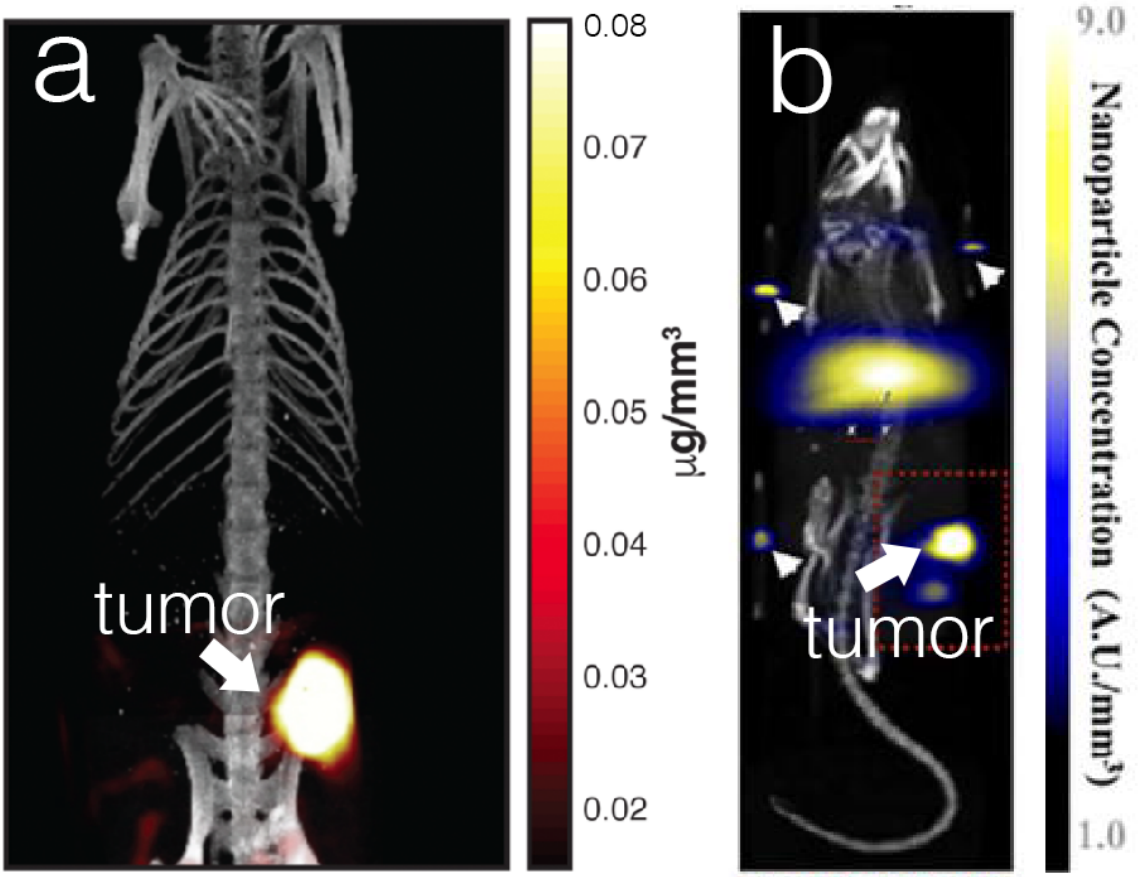

Figure 2.3: Cancer Imaging in MPI. (a) Imaging of xenografted breast tumor in rats. Image is 6-hr post-injection. Experiment took advantage of the EPR effect to passively target tumor. 3D MPI image with 4 x 4 x 5.8 cm FOV with CT skeletal reference. Magnetic Gradient of 7 x 3.5 x 3.5 T/m. Reprinted (adapted) with permission from [12]. Copyright 2017 American Chemical Society. (b) Imaging of brain cancer xenografts using active targeting of cancer by conjugated lactoferrin nanoparticles. MPI images were acquired with Magnetic Insight Momentum MPI scanner with gradient strength of 6 x 6 T/m gradient with 6 x 8 cm FOV. [13] republished with permission of Royal Society of Chemistry; permission conveyed through Copyright Clearance Center, Inc.

with MPI signal, just a lesser amount. No comparison was done between functionalized and non-functionalized nanoparticles.

A fundamental challenge with the EPR effect was highlighted by Wilhelm at al. [17]. The group showed that less than 1% of targeted nanoparticles actually reach targeted tumor cells. They found that 99% of nanoparticles injected were taken up by organs like the liver and spleen [17]. Of those that made it to the tumor, the majority were in the extracellular matrix or taken up by perivascular tumor-associated macrophages [18]. However, in terms of imaging the location of the tumors, rather than delivering chemotherapeutic drugs, it could be argued that nanoparticles surrounding tumor cells is sufficient for imaging purposes. MPI is very promising in this regard.

Another potential targeting pathway for MPI that would not require the EPR effect to be effective is selectin targeting. Selectins are cell surface peptides that mediate the adhesion of white blood cells to vascular walls under flow [19]. They play an integral part of the metastasis process, recruiting tumor cells into the vasculature [20]; circulating tumor cells, like leukocytes, roll across endothelial surfaces [21]. E-selectin targeting has been successfully demonstrated with superparamagnetic iron oxide nanoparticles in MRI [22]. We believe that E- and P-selectin targets SPIOs could be very promising probes to image cancer with MPI.

Others in the field [23] have used MPI to track cells for cancer imaging. Their work shall be addressed in the next section, as motivation for MPI cell tracking.

2.1.2.2 Cell Tracking in MPI

White blood cell (WBC) tracking using MPI is of note due to the explosion of interest in immunotherapy [23, 25–29]. Immunotherapy treatments for cancer are based on the concept of immune surveillance, where the immune system can identify and eliminate, with high specificity, cancerous cells before they cause harm within the body [30]. As such, immune cells are naturally drawn to the site of cancerous tissue and can be armed for its destruction. Monitoring immune cells and their migration is essential for evaluating cancer immunotherapies.

Imaging techniques like ^{111}Indium scintigraphy help doctors visualize WBC hotspots within the body. There is enormous interest in tracking CAR-T and CAR-NK immunotherapies. However, T cells and NK cells are both very radiation sensitive. Note that the radiation does to the WBCs themselves is much higher than to the patient. The 70-kg patient's radiation dose during a ^{99m}Tc or ^{111}In WBC scan is initially administered to a tiny ($\sim$70 mg) mass of WBCs prior to autologous reinjection. This 1-million-fold high radiation dose to WBCs can kill WBCs, adversely affecting targeting efficacy and specificity [31]. CAR-T and CAR-NK cells cannot survive this radiation dose [32, 33]. MPI has great potential as a cell tracking imaging modality due to its long lasting, non-radioactive tracers [5].

MPI has been used to track circulating tumor cells, neutrophils, and dendrites [23, 26, 27]. Parkins, et al. [23] used the concept that circulating tumor cells can home back to their primary tumor site to image xenografted mammary fat pad tumors, which were detected at the tumor site 72 hours following intracardial injection. Chandrasekharan, et al. [27] used

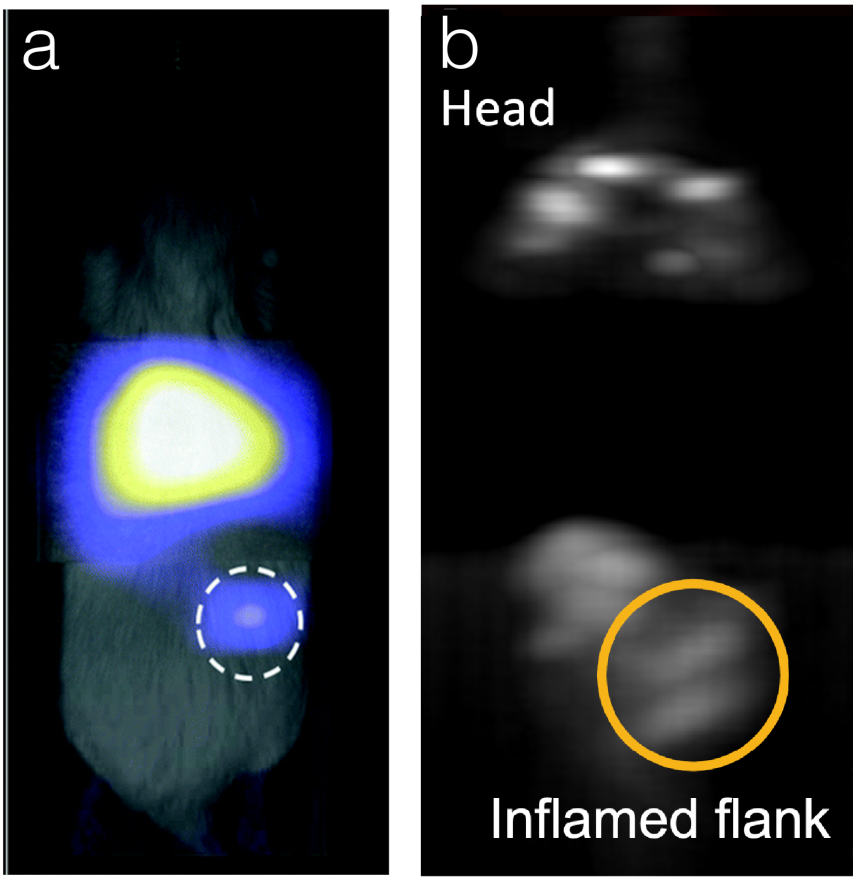

Figure 2.4: MPI Cell Tracking Applications (a) MPI image of 5 x 10^5 Micro-sized iron oxide particle (MPIO) labeled circulating tumor cells. Labeled cells were detected in the mammary fat pad tumor on the mouse's right flank, 0.8 $\pm$ 0.2 μg per tumor. 3D images were collected on a Momentum^{TM} (Magnetic Insight, Alameda, CA, USA) scanner with a 3 T/m gradient and a FOV of 12 x 6 x 6 cm with a total scan time of 1 hr. Republished with permission of Royal Society of Chemistry, [23]; permission conveyed through Copyright Clearance Center, Inc. (b) Anterior-Posterior maximum intensity projection of 3D MPI data, imaging a mouse with lipopolysaccharide endotoxin induced muscle inflammation in the right leg. Scans were collected on a 6.3 T/m field-free line scanner with 2D Projections with a 10.6 x 6.2 cm FOV. Reprinted with permission from [24]; permission conveyed through Copyright Clearance Center, Inc.

antibody-conjugated nanoparticles for *in situ* labeling of neutrophils and monocytes, then tracked these cells to sites of infection and inflammation. These scans had a contrast-to-noise ratio of 8-13 in the site of inflammation. Gevaert, et al. [26] tracked dendritic cells to popliteal lymph nodes after being injected into murine footpads. Within 2 days, each mouse showed cell migration to at least one of the targeted lymph nodes, though only 2-3% of the dendritic cells migrated. However, this was still able to be visualized using MPI.

MPI has also been used with great success for stem cell tracking within the body. Stem cell therapies have enormous potential, with over 14 diseases and injuries about to reach clinical trials [34]. However, successful implementation of stem cell therapies requires better understanding of cell fate after implantation. The stem cells must reach their intended targets, remain there, and maintain viability [35]. MPI has demonstrated success as a stem cell tracking and implant monitor.

MPI has tracked neural stem cell implants in mice and rats, tail injections of stem cells in rats, and implants in mice flanks [5, 6, 36, 37]. Zheng, et al. [5] demonstrated that MPI tracked stem cell implants for up to ninety days after their implantation. The group also showed a 200-cell sensitivity. This is an improvement over previous cell tracking efforts in nuclear medicine. SPECT and scintigraphy scans can often only track cells for hours. In 2016, Zheng et al. [6] showed that stem cells injected intravenously lodge themselves in the capillary bed of the lungs. Intravenous injection is a technique commonly used in clinical trials for administration of stem cells [38, 39]. Zheng et al.'s results thereby show the ineffectiveness of the technique for stem cell delivery to the appropriate tissues. Neural stem cell implants were tracked by Bulte, et al. [40], but only a detection limit of 10^4 cells was found. Both Bulte et al. and Sehl et al. [37] found that MPI is comparable to ^{19}F MRI for cell tracking applications. In every case, MPI was found to successfully track stem cells.

MPI has many strengths that lend themselves well for cell tracking applications. MPI can easily label phagocytic cells, e.g., dendritic and stem cells. Nanoparticles can also be functionalized to label cells like neutrophils *in situ*. These strengths, along with the other strengths of MPI mentioned previously, make MPI an excellent choice for cell tracking applications. In addition to MPI's capabilities for cell tracking, SPIOs have been shown to minimally affect gene expression in stem cells [40], a trait that is not shared by nuclear medicine, which damages cell function and their viability [41]. These examples make it clear that MPI is well suited for cell tracking throughout the body.

2.1.2.3 Vascular Imaging in MPI

MPI has great potential for imaging small, active bleeds in the body. No current clinically-used technique for bleeds, no matter where they are in the body, is very sensitive for small bleeds. Gut bleeds are typically imaged using ^{99m}Tc red blood cell (RBC) scintigraphy, a process where red blood cells are withdrawn from the body and labeled with radionuclides. They are then re-inserted in the body and their location tracked in a scintigraphy scan. This ^{99m}Tc scan requires a bleed of 3-5 mL of blood volume to image [42]. Traumatic brain injuries and intracranial hemorrhages are typically imaged with CT scans. Mild traumatic

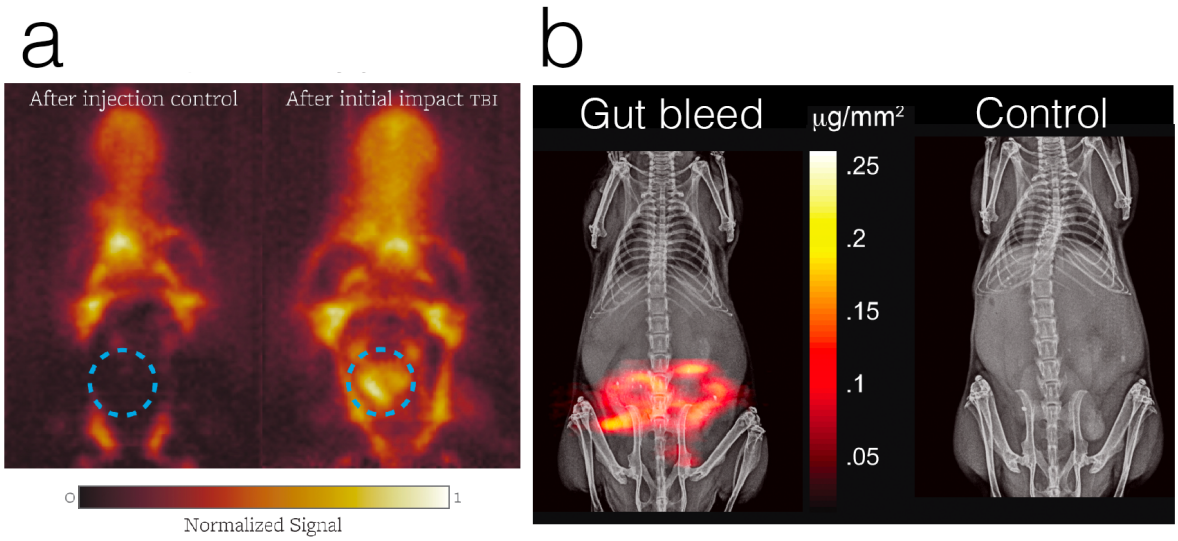

Figure 2.5: Vascular imaging in MPI. (a) Traumatic brain injury (TBI) imaging of rats. The blue dotted circle indicates area of impact. Unlike the control, the TBI has significantly more signal at the site of impact, which is representative of an intracranial bleed [44]. Maximum Intensity Projection of 3D scan. Gradient strength 7 x 3.5 x 3.5 T/m. FOV is 4.0 x 3.75 x 8.75 cm with a 10 minute acquisition. Republished with permission of IOP Publishing, Ltd, [44]; permission conveyed through Copyright Clearance Center, Inc. (b) MPI imaging of a gut bleed in mice. Gut bleeds were induced by introducing heparin to Apcmin/+ mice. Gut bleed was visualized by digital subtraction of the first time point measurement from the subsequent measurements. Twenty-one projection scans were taken over the course of 130 min. 2D Projection scan with 6.3 T/m gradient. FOV was 5.16 x 8.52 cm. Reprinted (adapted) with Permission from [45]. Copyright 2017 American Chemical Society.

brain injuries with their potential for bleeds are often not considered for imaging at all [43]. MPI with its 5 ng of Fe per voxel sensitivity is well suited to imaging small bleeds [5].

Circulation time poses one of the most crucial issues for MPI's vascular imaging. This is the time that nanoparticles circulate throughout the body before they're taken up by the body's reticuloendothelial system. Circulation time depends on the type of particle used, most specifically, their coating [46]. Nanoparticle coating has a sizable effect on their function and purpose. For example, in Szwargulski, et al. [47], the use of the tracer Perimag with a coating of dextran decreased their abilities to visualize intracranial bleeds. One commercially available particle, Resovist, with a coating of dextran, had nanoparticles taken up by the liver and spleen within minutes of injection [48]. The Krishnan group at the University of Washington, created their own particles with polyethylene glycol (PEG) coatings, which had a half-life of 4.2 hours [49]. Vascular imaging with MPI requires long-circulating tracers

because most relevant MPI applications, other than those that take place in the liver, require more than minutes to traverse the body and highlight bleeds.

As a blood pool tracer with long-circulating nanoparticles, MPI has a proven track record of successfully imaging traumatic brain injuries, intracranial hemorrhages, and gut bleeds [44, 45, 47]. Yu et al. [45] detected bleeds of 2 μL of blood extravasating the gut lumen in one voxel. Orendorff, et al. [44] visualized traumatic brain injury in a mouse for 11 days after the injury occurred. Szwargulski, et al. [47] detected a tracer bolus representing an intracranial hemorrhage in less than 3 minutes. These applications demonstrate MPI's high sensitivity to small active bleeds.

2.1.2.4 MPI Hyperthermia Imaging

MPI shows promise for "focusing" magnetic fluid hyperthermia (MFH), a therapy which deposits heat to irreversibly damage pathological targets. In MFH, thermal energy accumulates by AC magnetic fields rapidly changing the magnetization of pre-injected magnetic nanoparticles. This preferentially damages cancerous tissues, which are more sensitive to heat than normal tissues [50]. Brown et al. showed that cancerous tissues showed damage at twice the rate of normal tissue. However, these magnetic nanoparticles, if introduced systemically, can end up in other heat-sensitive tissues in the body, e.g., the liver, due to their preferential uptake of nanoparticles within the body [51]. This explains the need for some sort of "focusing" in MFH.

"Focusing" with MPI depends on gradient placement, not on AC magnetic field focusing. AC magnetic fields cannot be focused to more than half of their wavelength; relatively low-frequency magnetic fields have wavelengths larger than the human body. For example, a 300 kHz focused magnetic field in tissue has a wavelength of 55 m. The inability to focus AC magnetic fields to the scales needed activates all the nanoparticles within the body, which can cause damage to healthy tissue [53]. MPI gradients, on the other hand, can be used for localization in magnetic hyperthermia, just like they are used for localization in MPI. Generally, magnetic nanoparticles affected by gradient magnetic fields are locked into alignment and cannot rotate with applied AC magnetic fields. Hence, they cannot deposit energy and heating to untargeted tissues [52]. This combination of MPI and magnetic hyperthermia overcomes one of the greatest problems in magnetic hyperthermia, that of focusing heat production within the body. Fig. 2.6 shows this localization of heating.

Success for MPI-MFH depends on a combination of scanner design and tracer design. Baeur et al. [54] introduced tracers designed for dual purposes (imaging and hyperthermia) in the form of zinc-doped magnetite cubic nanoparticles with showed a 5-fold improvement in SAR while showing a resolution comparable to ferumoxytol. Hensley et al. [55] designed a combined MPI-MFH system that provided selective heating of samples separated by 3 mm. Tay et al. [52] then used the previously-designed MPI-MFH system [55] to localize selective heating in a two xenografted tumor murine model. As seen in Fig. 2.6 the bottom tumor, which was treated using MFH, was no longer viable. The top tumor was not affected by this treatment. The MFH studies developed with MPI could be used to clinically treat

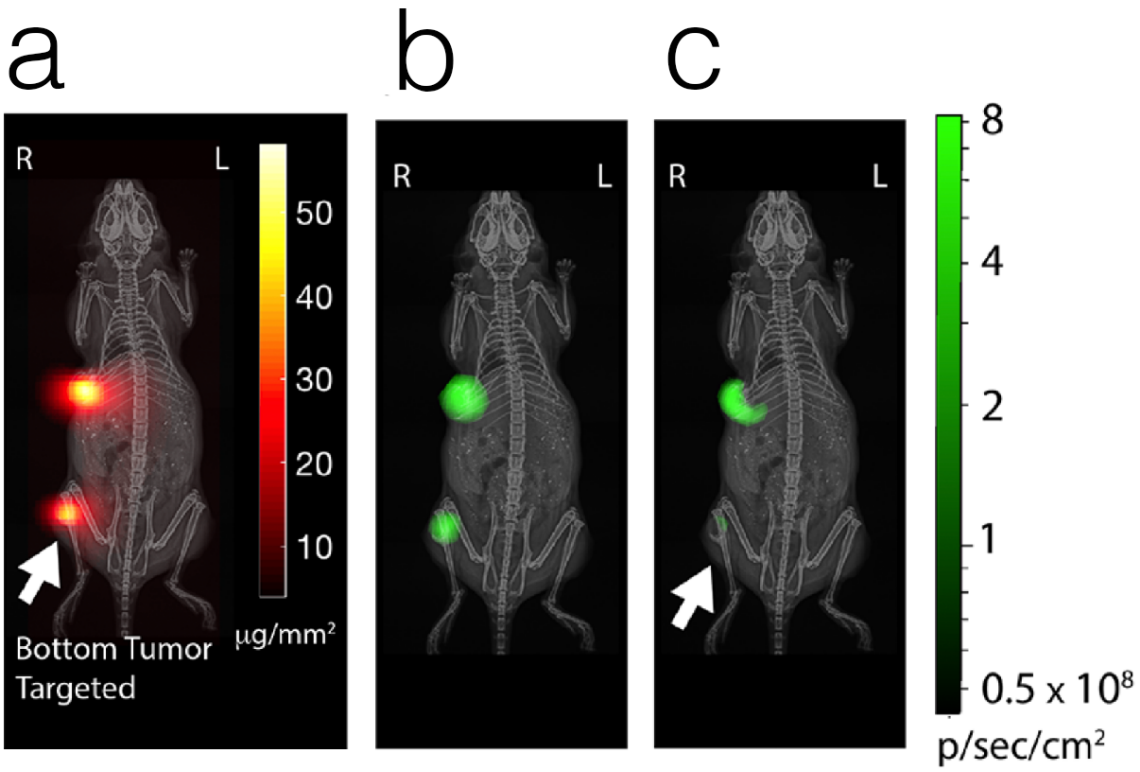

Figure 2.6: Hyperthermia in MPI. Xenografted bioluminescent tumors implanted in right flank and right side of mouse torso. Gradient localized heating targeted the bottom tumor, and, after 3 days post treatment, the bottom tumor underwent apoptosis. Bioluminescent imaging was obtained via an IVIS Lumina system with auto exposure time and medium binning. Mice were imaged in 3D Projection MPI scanner with 6.3 T/m gradient. The FOV was 12.35 x 4.75 x 4.75 cm with a scan time of approximately 2 minutes. Localized Heating of SPIOs took place with a specialized scanner with a 2.35 T/m gradient, with 30-60 min of heating time. Reprinted (adapted) with permission from [52]. Copyright 2018 American Chemical Society.

cancers such as prostate cancer and glioblastoma with much finer heating resolution than MFH alone.

2.2 MPI Imaging Theory

This section will cover how images are made in MPI. I will describe MPI physics, signal generation, and how these signals are reconstructed. Then, I will touch upon the physics that causes blurring in MPI, magnetic relaxation.

2.2.1 MPI Physics and Signal Generation

MPI directly measures the nonlinear electronic magnetization of SPIOs, superparamagnetic iron oxide nanoparticles. SPIOs are typically made of magnetite (Fe_3O_4) and are 30 nm or less in diameter. This size restriction allows for magnetite, typically ferrimagnetic in sizable quantities, to behave as single-domain paramagnetic nanoparticles. Their magnetization is much stronger than typical paramagnets because they are single magnetic domains, hence the term superparamagnetic.

The Langevin equation describes the magnetization for a non-interacting ensemble of SPIOs as function of the applied magnetic field [56]. The magnetization of the system is equal to the following equation, where N is the number of particles per volume ($\#/m^3$), m is their individual magnetic moment (Am^2), and k (m/A) is the ratio of the magnetic moment of an individual particle and the thermal energy of the system:

$$\begin{aligned} M(H) &= NmL(kH) \\ &= Nm\left(coth(kH) - \frac{1}{kH}\right) \end{aligned} \tag{2.1}$$

Fig. 2.7 shows the Langevin equation and its effect on MPI images. Fig. 2.7 (a) and (b) shows the Langevin function and the effect an applied field has on a SPIO's magnetization. Fig. 2.7 (c) shows how an applied magnetic field affects the inductive measurement of the SPIO's magnetization.

MPI then takes advantage of the nonlinear magnetization of SPIOs to localize the MPI signal within the field-of-view (FOV) of a scanner. To do so, large gradient magnets are placed on either side of the FOV. Their magnetic fields repel one another such that there is a region between the two gradient magnets where no magnetic field is felt. This region is called the field free region (FFR). Fig. 2.8 shows such a design. Two dynamic, spatially homogeneous fields (one fast, one slow) allow us to shift the instantaneous FFR across the FOV, enabling localization of signal.

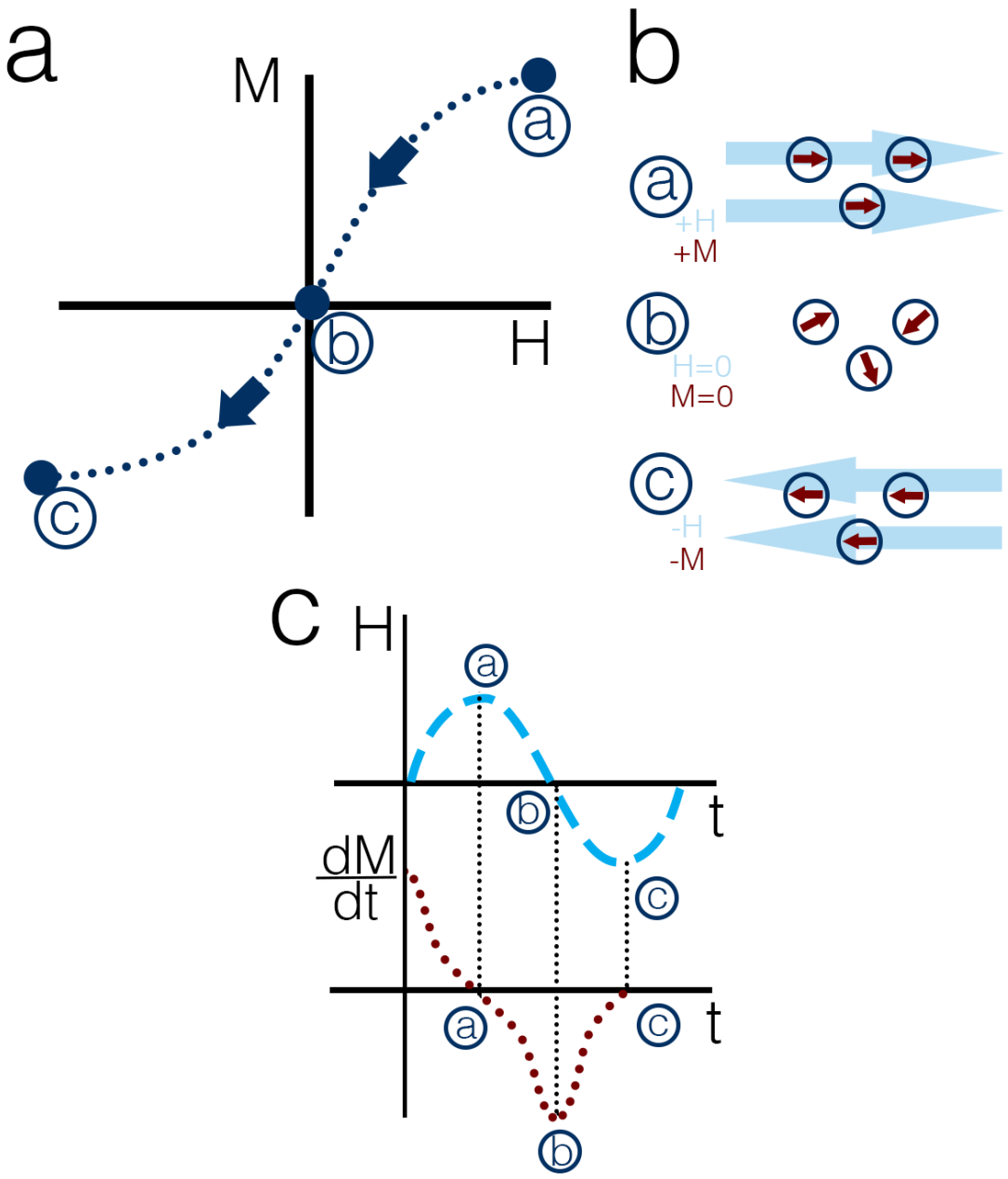

Figure 2.7: Superparamagnetism and its effect on MPI images. (a) The Langevin curve personifies the magnetization of superparamagnetic nanoparticles. (b) The magnetization of superparamagnetic nanoparticles saturates with positive and negative magnetic fields, but the net magnetization is zero with no magnetic field. (c) Inductive sensing of changing magnetization creates the MPI point spread function (PSF), which determines the resolution of the modality.

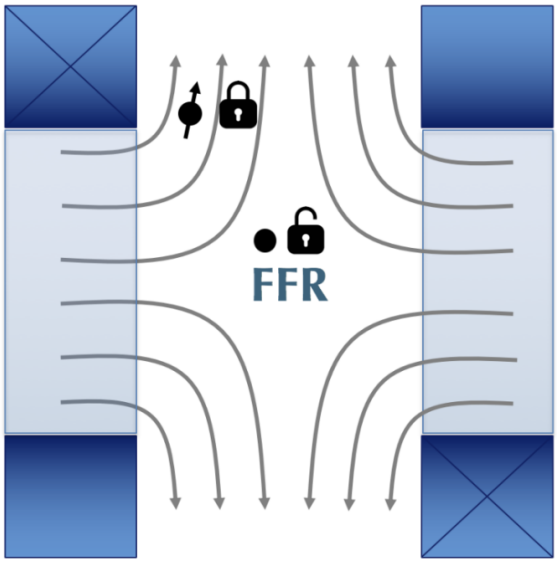

Figure 2.8: MPI Scanner FOV. On the left and right are two gradient magnets with opposing magnetic fields. SPIOs that are aligned with the gradient magnetic fields are locked into place and cannot be sensed inductively. Only SPIOs within the field free region, FFR, can be sensed inductively, therefore localizing the MPI signal.

2.2.2 MPI Image Reconstruction

This section discusses spatial encoding and image reconstruction in MPI. X-space reconstruction is a gridding operation dependent on knowing the position of the FFR. As said earlier in Section 2.2.1, MPI requires a gradient magnetic field to localize the FFR and encode the spatial position of nanoparticles within the FOV. All the particles within the sample experience a gradient field and an applied field

$$H(x,t) = -Gx + \frac{B_{ex}}{\mu_0} cos(2\pi f_0 t) \tag{2.2}$$

Where G is the strength of the gradient field, B_{ex} is the amplitude of the applied field, μ_0 is the permeability of free space, and f_0 is the frequency of the sinusoidal applied field [4]. Solving for the position of the FFR, where the applied magnetic field is zero, we find that the equation for the FFR is

$$x_s(t) = \frac{B_{ex} cos(2\pi f_0 t)}{\mu_0 G} \tag{2.3}$$

showing that the FFR trajectory is sinusoidal and the amplitude, or, width of the trajectory, is $\frac{B_{ex}}{\mu_0 G}$ [4]. The width of the trajectory is proportional to the amplitude of the applied

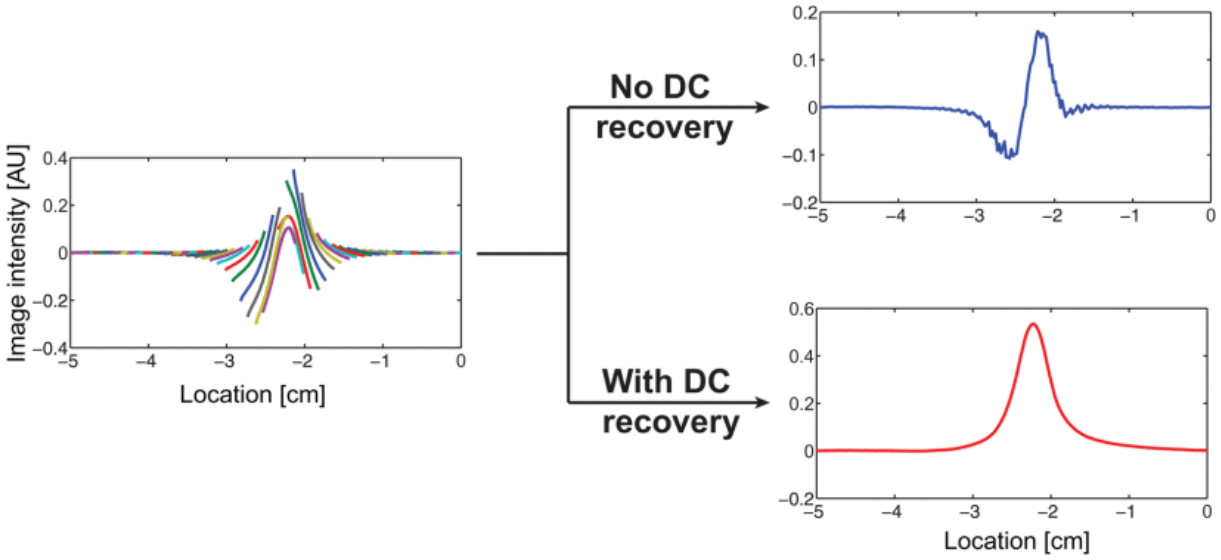

Figure 2.9: Experimental data of MPI images reconstructed with and without DC recovery. The reconstructed image without DC recovery has a very different shape from the ideal image and is not quantitative. Reprinted, with permission, from [4]. IEEE ©2013.

field and inversely proportional to the strength of the gradient field. MPI signals are sensed inductively; the measured voltage is the product of the coil's sensitivity and the changing flux through the coil. This is shown in the voltage equation, $EMF(t) = -B_1 \frac{d\Phi}{dt}$, where Φ is the magnetization of the nanoparticles through the coil. The signal equation for MPI at the FFR is [57]

$$s(t) = \rho(x) * \dot{L}[kGx]\Big|_{x=x_s(t)} B_1 mkG\dot{x_s}(t) \tag{2.4}$$

To find the native distribution of the nanoparticles, $\dot{x_s}(t)$ must be removed from the measured signal. The benefit to this operation is that it only requires a single division per position of the FFR and the gridding of that position, all of which can be achieved in real time.

Another challenge in reconstruction is eliminating the direct feedthrough that is inherent in MPI. Direct feedthrough is a natural byproduct of the receive coil measuring both the transmitted magnetic field and the magnetization of the sample at the same time. In the frequency domain, direct feedthrough only contaminates the first harmonic of the receive signal because the transmitted signal is a pure sinusoid. There is near-zero direct feedthrough at higher harmonics. Hence all MPI scanners reject the signal at the first harmonic with an analog filter. This direct feedthrough rejection filter kills both the direct feedthrough interference (intentionally) and the first harmonic signal from the SPIOs (unintentionally).

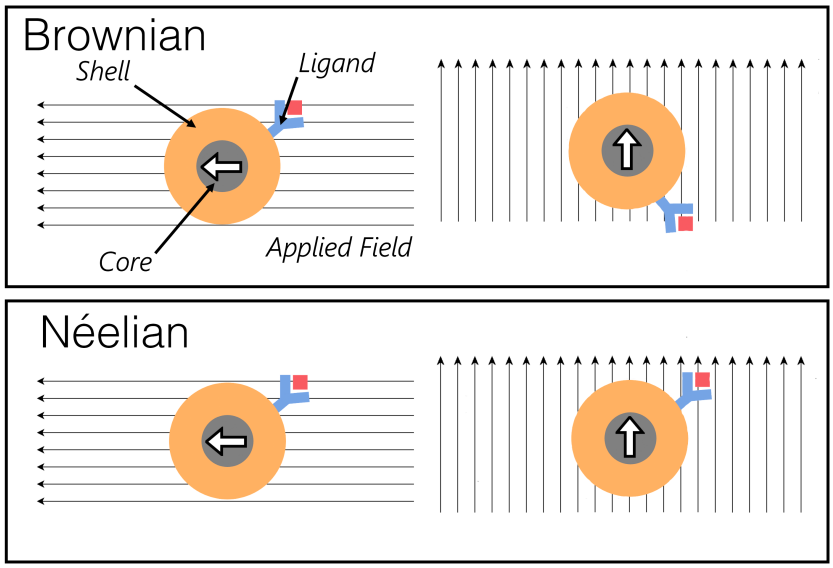

Figure 2.10: Nanoparticle Magnetic Relaxation. The top figure shows Brownian relaxation, where the magnetic moment of the SPIO aligns with applied magnetic fields by physically turning, as shown by the attached antibody turning with the magnetic moment. The bottom figure shows Néel relaxation, where the magnetic moment aligns with applied magnetic fields within its crystal structure, as shown by the attached antibody remaining in the same position.

Reconstructing the MPI scan given only the higher order harmonics is the inverse problem challenge in MPI.

Fortunately, Lu et al. [4] showed that the lost first harmonic signal corresponds to a loss of the center of k-space (or DC) value of a partial FOV scan. Lu found that the lost partial FOV DC signal can be restored with a robust algorithm that enforces image continuity and zero signal outside the FOV. Without Lu's algorithm, an incorrect PSF is reconstructed, as seen in Fig 2.9. Enforcing these *a priori* assumptions allows the DC signal to be effectively recovered.

2.2.3 Magnetic Particle Relaxation

All the previous statements about MPI physics and signal generation operates under what is called an adiabatic assumption, the assumption where no energy is lost in the system. The adiabatic condition assumes that each SPIO instantaneously follows the applied magnetic field. However, in reality, the alignment does not occur instantaneously; that process is called magnetic relaxation. Relaxation can occur by two mechanisms: Néel relaxation and

Brownian relaxation. MPI obeys Debye physics, and so the observed magnetization is well modeled as the adiabatic magnetization waveform temporally convolved with a relaxation kernel, as seen in the following equation [58]:

$$M(x,t) = M_{adiab}(x,t) * \frac{1}{\tau} e^{-t/\tau} u(t) \tag{2.5}$$

where τ can be either Brownian or Néelian relaxation. The two relaxation mechanisms occur in parallel and so we measure the faster of the two. Relaxation slows down the inductive sensing of the MPI signal and adds blur to the image.

2.2.3.1 Néel Relaxation

Néel relaxation describes the realignment of the nanoparticle's magnetic moment within its crystal structure [59]. The time it takes for Néel alignment to occur is described with the following equation

$$\tau_N = \tau_0 \frac{e^{\rho}}{\sqrt{\rho}} \tag{2.6}$$

where

$$\rho = \frac{KV_m}{k_B T} \tag{2.7}$$

where τ_0 is a constant, 10^{-9}s, V_m is the volume of the magnetic core of the nanoparticle, and K is the anisotropic energy constant, which depends on the nanoparticle's crystal symmetry [56, 60, 61]. The ρ term defines the equation for the Néel relaxation constant and balances the thermal energy of the system and its anisotropy energy. As the volume of a nanoparticle increases, so does the Néel relaxation term, until the magnetization of the nanoparticle is locked into alignment and cannot be adjusted in any manner other than Brownian relaxation [61].

2.2.3.2 Brownian Relaxation

When the Néel relaxation time constant takes too long to align through the crystalline structure, the nanoparticle physically rotates with the magnetic field in Brownian relaxation. There is, of course, resistance to that rotation in the form of drag. This defines the Brownian relaxation constant as

$$\tau_B = \frac{3\eta V_H}{k_B T} \tag{2.8}$$

where η is the viscosity of the solvent surrounding the nanoparticle and V_H is its hydrodynamic volume. τ_B is the ratio of the thermal energy of the system to the resistance of motion resulting from physically rotating in a solvent.

2.2.3.3 Parallel Competition for Dominance

Nanoparticles within a fluid experience both Néelian and Brownian relaxation mechanisms. These two relaxation mechanisms act in parallel, and so, depending on the nanoparticle's crystalline or hydrodynamic properties, the fastest relaxation mechanism dominates [61]. Bear in mind that Néelian relaxation time increases exponentially with the magnetic core volume of a particle. Therefore, the larger a particle is, the more likely it is be dominated by Brownian relaxation.

2.3 Current challenges in MPI

It is challenging to scale up an MRI or an MPI scanner from preclinical to clinical sizes. MPI's clinical translation depends on scanner *and* tracer properties. Its current spatial resolution is not sufficient for its future clinical use. In this section, I will discuss the requirements necessary for clinical MPI scanners to occur.

As stated previously, Magnetic Particle Imaging inductively senses the changing magnetization of SPIOs. Because inductive sensing is defined by Faraday's Law, where the derivative of a changing magnetic field induces a voltage in a receive coil, MPI measures the derivative of the changing magnetization of SPIOs. The spatial resolution and signal-to-noise ratio (SNR) of an MPI signal is directly proportional to the speed at which the SPIO traverses the M-H curve.

The resolution for MPI is determined by its point spread function (PSF). Eq. 2.4 describes the signal equation for MPI. The resolution of the PSF is the most commonly evaluated with the Houston criterion. We calculate the full width half max (FWHM) spatial resolution using the distance between two points on the PSF that are one-half the peak maximum amplitude. This gives us the following equation for the spatial resolution (FWHM) of an MPI scan:

$$\Delta x = \frac{24 k_B T}{\mu_0 \pi M_{sat}} \frac{1}{G \cdot d^3} \tag{2.9}$$

where μ_0 is the permeability of free space, k_B is Boltzmann's constant, M_{sat} is the saturation magnetization of the ensemble of nanoparticles, and d is the magnetic core diameter of the particles. This equation shows us that there are two ways in improve the spatial resolution of our MPI scanner: the magnetic core diameter of our nanoparticles or the strength of the gradient field. One is determined by tracer properties, the other by scanner properties. Gradient strength for MPI is limited by cost, power, and cooling constraints. One reason is that the cost of the magnets quadratically increases as the gradient strength increases.

If gradient strengths cannot be increased, that leaves finding a higher resolution tracer. Currently, a pre-clinical MPI murine scanner using ferumoxytol nanoparticles (FDA approved [62]) has a spatial resolution of 5 mm using a 6 T/m gradient with a 4 cm bore radius [63]. A human-sized MPI scanner operating with a 1.0 T/m gradient using ferumoxytol would offer roughly 30 mm spatial resolution, which is not competitive with other

modalities. It is clear we need a higher resolution MPI tracer for human applications. The next chapter shall address past work to improve MPI resolution with unique tracer physics.

The bulk of the dissertation describes experiments investigating the fundamental nanoscale physics mechanism of superferromagnetic behavior. I developed a unique pulse sequence to measure the transition time of superparamagnetic iron oxide nanoparticles to superferromagnetic iron oxide nanoparticles. I measured this transition as a function of transmit amplitude, particle concentration, and solvent viscosity. My work has led to greater understanding of SFMIO behavior and will inform future projects on SFMIO biocompatibility and safety.

Chapter 3

Search for Improved MPI Spatial Resolution

In this section, I describe MPI's search for better spatial resolution along two paths: the synthesis of optimized nanoparticles and the development of reconstruction algorithms and pulse sequences to overcome magnetic relaxation. High-resolution nanoparticle synthesis for MPI has focused on developing larger single-core magnetite tracers. However, Tay et al. [64] and Croft et al. [58] showed magnetic relaxation thwarts the expected resolution gains from these particles. Many groups [65–68] designed pulse sequences to overcome magnetic relaxation and reclaim the expected resolution improvements. The new combination of these pulse sequences and superparamagnetic nanoparticles has driven MPI within close reach of its resolution limit using SPIOs.

3.1 MPI's search for improved spatial resolution

Magnetic Particle Imaging (MPI) is a unique, relatively new *in vivo* imaging modality. Its physics, e.g., zero signal attenuation and positive contrast, set it apart from other imaging modalities. However, a huge concern for MPI's clinical translation is its spatial resolution. MPI scanners have achieved head-size scale for cerebral blood volume applications [69]. Using non-FDA approved nanoparticles optimized for MPI, this scanner reached a spatial resolution of 7 mm with a gradient strength of 1.5 T/m[69]. This resolution is comparable to functional MRI, but CT and MRI would outcompete MPI for angiography and stroke imaging with their in-plane resolution of $\sim$1 mm. More work must be done to make MPI human scanners feasible. Barring an unrealistic increase in gradients used in scanners because of the need for cryogenics [70], tracer optimization is the most promising course forward.

3.2 Current State of Superparamagnetic Nanoparticles in MPI

In general, MPI uses superparamagnetic nanoparticles as tracers within the body. Use of these nanoparticles for liver imaging, an off-label use, in Magnetic Resonance Imaging (MRI) occurred as early as 1989 [71]. The first use in humans visualized the presence of malignant tumors in the liver. SPIOs were uptaken by healthy tissue but not by cancerous, thus creating the contrast needed for tumor visualization [72]. While MPI works with SPIOs that are traditionally used as contrast agents in MRI, specially designed nanoparticles are much more successful. The former tend to be multiple small particles bound together in a cluster by a particle coating such as carboxydextran (multi-core), and the latter tend to be single-core nanoparticles.

Table 3.1: Commonly Used Nanoparticles for MPI

Iron Oxide	Marketing Status	Core Diameter (nm)	FWHM (Δx in mm)	MPI sensitivity (ng Fe)
Resovist® Bayer	Approved for Clinical Use in EU/Japan	3-5 clustered	1.37	11.9
Feraheme® AMAG Pharma	Approved for Clinical Use by FDA	6-7 clustered	5.64	77.22
Vivotrax™	Research use only	4.2	1.63	18.54
Lodespin Lab (LS-017)	No longer available	28.7	0.83	3.0

Sources: [70]
Assumed gradient strength was 7 T/m.

Table 3.1 shows four common MPI tracers and their performance. Resovist and Vivotrax are the most common and consist of small clustered nanoparticles bound together in carboxydextran [48]. Resovist is commonly used despite Resovist nanoparticles being responsible for only 3% of MPI signal in a sample [1]. Feraheme can be used for MPI [63] but suffers from a significant decrease in particle resolution. Lodespin Lab's LS-017 is representative of the monodisperse magnetite tracers for research use that produce the best resolution for MPI, but Lodespin Labs tracers are no longer available commercially.

3.2.0.1 An aside: FDA black-box warning

Superparamagnetic iron oxide tracers are still used as contrast agents in MRI clinically, but not without reservations. Only one MPI tracer, Feraheme, or ferumoxytl, is currently FDA approved [73, 74], but only as an intravenous medication to treat iron-deficiency anemia in patients with chronic kidney disease [75, 76]. Patients experiencing adverse events due

to Feraheme has led to a black-box warning on its use in the US. 79 cases of anaphylactic shock led to 18 cases of death with the first dose of ferumoxytol [77], and the tracer is administered over half a million times in a typical year [78]. This makes ferumoxytol's rate of anaphylactic shock higher than every other intravenous iron tracer on the market [78]. Physicians are warned of its potential side effects [77], yet many remain devoted to its off-label use as a contrast agent, given the use of trained personnel, monitoring equipment, and resuscitation supplies [79].

3.2.1 Synthesis of SPIOs

A background understanding of nanoparticle synthesis sheds light on how tracer dynamics affect the images created. MPI performance, sensitivity, and resolution strongly depend on the type of tracer, as shown in table 3.1. A clustered nanoparticle like ferumoxytol versus a single-core nanoparticle like LS-017 have a five-fold difference in resolution.

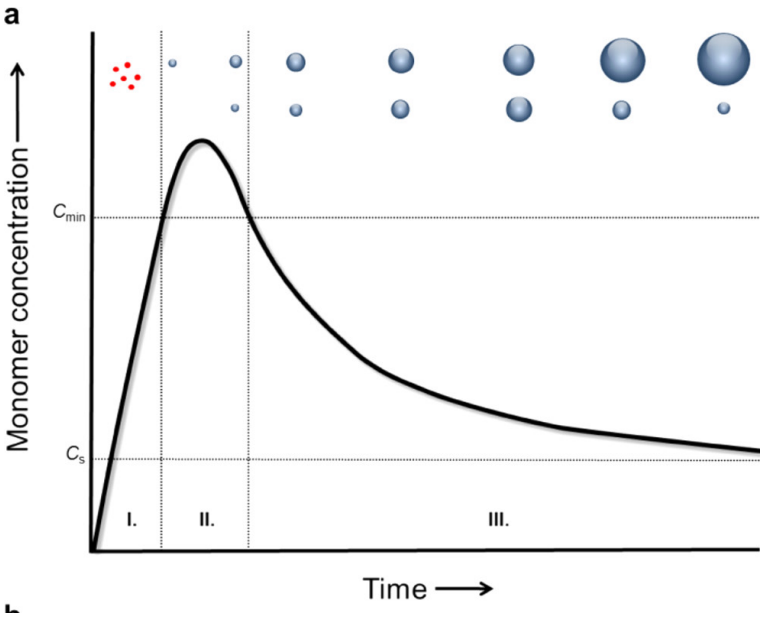

Figure 3.1: LaMer Mechanism showing the three stages of concentration rapid increase, nucleation, and particle growth. Reprinted with permission from [80]. ©2015 American Chemical Society.

The LaMer mechanism (Fig. 3.1) is commonly used to describe the relationship between a monomer (a reacted molecule dissolved in a solution) concentration versus time [80–82]. This mechanism can be described in three stages. During stage 1, the monomer's concentration rapidly increases to the point of supersaturation, but no particles are present. At stage 2, the monomer reaches the critical level of nucleation to generate particles, significantly

reducing the concentration of the free monomer in solution. From this point at stage 3, the nanoparticles grow in size without additional nucleation.

A challenge in nanoparticle synthesis is the wide range of nanoparticle sizes that can occur within a single reaction. One issue is that if the nucleation event is too low in Stage 2, a monodisperse distribution might not be obtained [83]. Another factor is that Ostwald ripening occurs in Stage 3. This is the process where large particles grow larger and smaller particles stay the same size. These factors, low nucleation events and Ostwald ripening, are generally considered to be why a large range in particle sizes often exists [80].

The synthesis process of SPIOs tends to indicate their success as tracers in MPI. The ideal MPI nanoparticles should have controlled size ranges to reduce the amount of relaxation blurring. Each different nanoparticle size has its own relaxation, both forms of which depend on magnetic particle volume. The core sizes should be as large as possible and single-core, as predicted by Langevin theory and MPI physics. Particles synthesized through the co-precipitation method tend not to perform as well in MPI because they generate a wide distribution of particle sizes, increasing relaxation blurring in MPI [61, 84]. Nanoparticles synthesized through thermal decomposition methods have been successful in MPI because of their size-controlled and single-core properties [85–87]. Fig. 3.2 shows the differences in particles produced by the two different methods.

3.2.1.1 Co-precipitation Method

Co-precipitation is the most likely method for creating the clinically used, non-ideal tracers, ferumoxytol and ferucarbotran [88]. Co-precipitation methods produce a large range of nanoparticle sizes with poor crystallization and irregular crystal shape [61, 89]. They can be described as colloidal nanoparticles [89]. These are not ideal for MPI because Langevin theory and MPI physics predict that size-controlled single-core magnetite nanoparticles make the best tracers. Still, this method is a fast and relatively simple way to produce a large amount of nanoparticles [61, 84], making it a reasonable method for creating clinical tracers.

The co-precipitation synthesis usually prepares nanoparticles by mixing ferrous and ferric salts in an aqueous medium at or above room temperature. The size and shape of the nanoparticles depend on many factors, e.g., reaction temperature and PH [84], and needs to occur in an oxygen-controlled environment to avoid the transformation of magnetite into maghemite [61]. The size of the nanoparticles must be determined during a very short nucleation period [61]. This tends to produce nanoparticles in size ranges from 2-15 nm [61]. These smaller particles are not ideal for MPI, where the resolution is inversely proportional to the magnetic core volume of the nanoparticle [57].

3.2.1.2 Thermal Decomposition Method

The control over size distribution in thermal decomposition enables ideal MPI tracers. Magnetite nanocrystals are prepared by decomposing iron-oleate complexes at above 300^o C in octadecene [90]. One of the most successful methods for size-controlled nanoparticles the

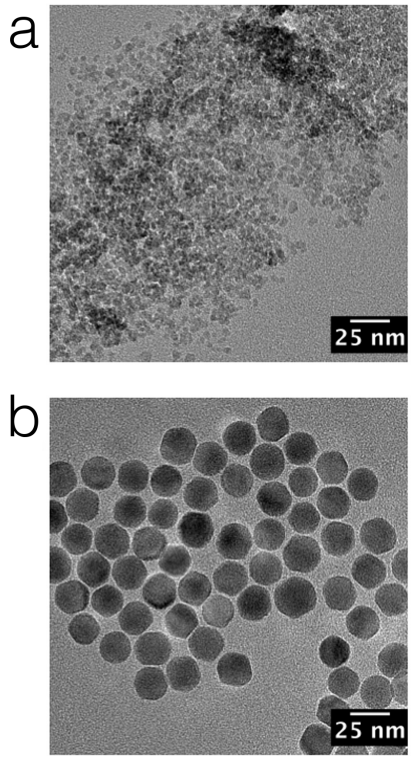

Figure 3.2: TEM of commercially produced nanoparticles, Resovist (a) and research-use thermally decomposed nanoparticles, from the University of Washington (b). Note the large change in particle size distribution and crystalline shape. Reprinted from [86], with the permission of AIP Publishing.

extended LaMer synthesis process. This process adds a constant drip of an iron-oleate precursor into an octadecene bath. The addition of solute in stage 3 of the LaMer process helps control Oswald ripening and confines nanoparticle size to 5-30 nm [80]. This size-control is essential for limiting relaxation processes such as Néel relaxation. The nanoparticles produced also have single-core crystalline structures, meaning that the spatial resolution improves as particle magnetic core size increases, according to the MPI signal equation [57].

3.3 Improving MPI resolution with superparamagnetic tracers

Langevin theory predicts that MPI resolution should improve as the magnetic core volume of a nanoparticle increases. However, this is an adiabatic prediction and does not include magnetic relaxation. The following sections will show how nanoparticle relaxation thwarts

that prediction. We will then discuss pulse sequences designed to overcome nanoparticle relaxation and restore MPI resolution to Langevin theory predictions.

3.3.1 The Relaxation Wall

Magnetic core size and relaxation have been of great interest to MPI researchers to improve MPI spatial resolution. MPI inductively measures the magnetization of nanoparticles such that the faster the magnetization of the nanoparticles in time, the steeper the PSF measured and the better the resolution of an MPI image. The equation for the resolution (FWHM) of MPI is seen in Section 2.3 and shows that the resolution of MPI's PSF is inversely proportional to the magnetic core volume of a tracer. This is most important for tracer design. Core size has been explored experimentally; researchers found that increasing nanoparticle core sizes improved MPI resolution, until relaxation begins to dominate [58, 86, 87]. Core shape has also been explored through modeling MPI spectra, showing that magnetic mono-domain particles were dependent on the anisotropy of the nanoparticles' magnetic core, thereby affecting a particle's Néelian relaxation [91]. The research supports the trend that core size and shape affect measured MPI signals, especially nanoparticle relaxation.

Magnetic particle relaxation is defined as the non-instantaneous response of a magnetic particle to the applied field [58]. The addition of relaxation effects causes an asymmetric blur based on the scanning direction. Intuitively, the blur makes sense: the position of the field-free region (FFR) can be represented as a sinusoid traveling from positive maximum excitation to negative maximum excitation as a function of time, as seen in Eq. 2.3. When inductive sensing measures the derivative of the magnetization as a function of time, we measure the change in the sample's magnetization as a function of applied field. Therefore, a positive-direction change in applied field, where the applied field goes from -B_{ex} to positive B_{ex} shows magnetic relaxation on the positive side of the PSF, as seen in Fig. 3.3.

The equations for the two forms of magnetic particle relaxation, Néelian and Brownian, are listed in Eq. 2.6 and Eq. 2.7, respectively. Both depend on the size of the nanoparticles, where Eq. 2.6 depends on the magnetic core volume, and Eq. 2.7 depends on its hydrodynamic volume. Both equations show improved resolution with increased nanoparticle core volume, but only to a certain point, the relaxation wall. At that point, magnetic relaxation dominates the signal and causes blurring.

Work by Tay, et al. [64] confirmed experimentally that magnetic relaxation dominates over any magnetic core gains. The group [64] used Imagion Biosystems PrecisionMRX© nanoparticles with core diameters from 18 to 32 nm and measured their PSFs. As predicted by the Langevin equation, they found that the resolution of the PSF improved up to a certain point, ∼24 nm, for these specific scanning parameters. After that point, magnetic relaxation was presumed to increased so that the resolution worsened. The observation that the Néelian relaxation constant exponentially increases with magnetic core size suggests that Tay et al.'s magnetic relaxation was Brownian. Tay, et al. [64] posited that the most promising approach for improving MPI resolution was optimizing nanoparticle size for maximum resolution and minimum relaxation-induced blurring. These results are seen in Fig. 3.4.

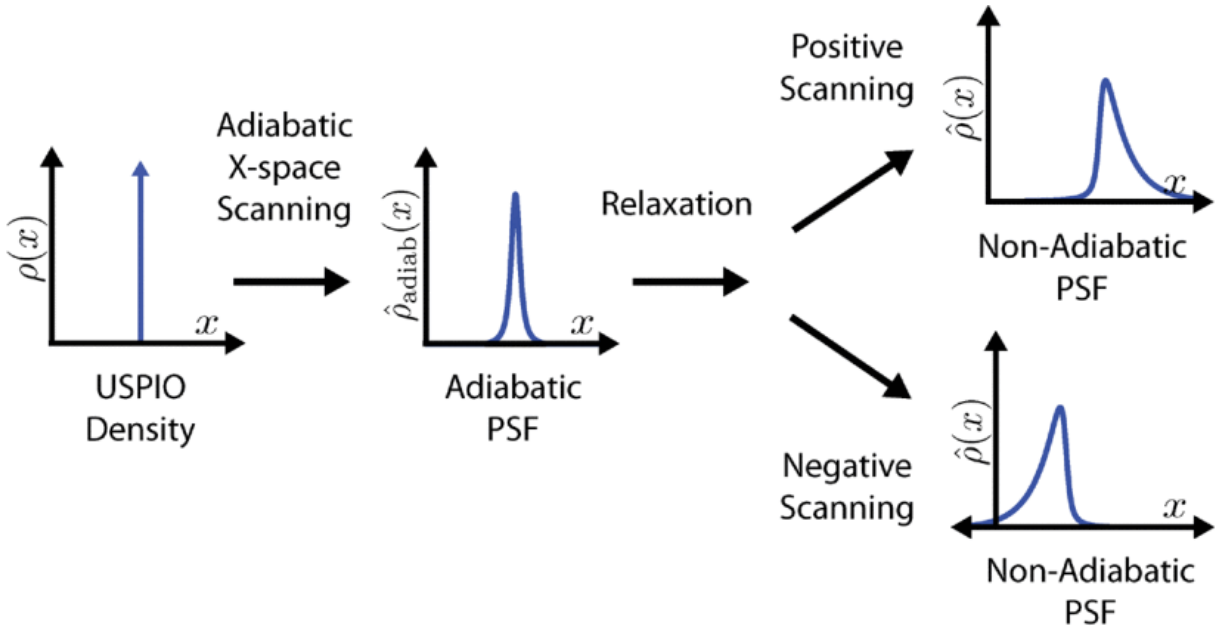

Figure 3.3: The left shows a delta function representing a point source of SPIO nanoparticles. That delta function is spatially convolved with the derivative of the Langevin function and the adiabatic PSF is produced. That PSF is the convolved with the temporal relaxation function, which causes asymmetric blurring in the PSF. Therefore, there are non-identical PSFs for the two scanning directions. Reprinted with permission of [58]. ©2012 IEEE.

3.3.2 Pulse Sequence efforts to mitigate Relaxation effects

Pulse sequences offer another path to mitigating relaxation blurring and maximizing spatial resolution. One of the most common strategies is low amplitude and/or low frequency approaches rather than the typical 20kHz, 20 mT pulse sequence most used for MPI [65, 68]. Low-amplitude and/or low-frequency pulse sequences greatly improve the resolution of MPI signals. They map the MPI signal to smaller locations in space, thereby reducing relaxation blur. The development of multi-frequency gradiometric relaxometers, most notably, the arbitrary wave relaxometer, have enabled pulse sequence development to flourish. Developed by Tay et al. [92], the AWR has opened the possibilities of new pulse sequences to explore how SPIOs respond to magnetic fields. This has greatly increased the number of frequencies and transmit amplitudes available to excite particles sinusoidally. It has also enabled the development of brand-new pulse sequences, such as square waveforms.

3.3.2.1 Arbitrary Waveform Relaxometer

As a reminder, the MPI receive coil picks up both the signal (EMF from the SPIOs) *and* the direct feedthrough interference coupled from transmitter to receiver (due to non-zero mutual

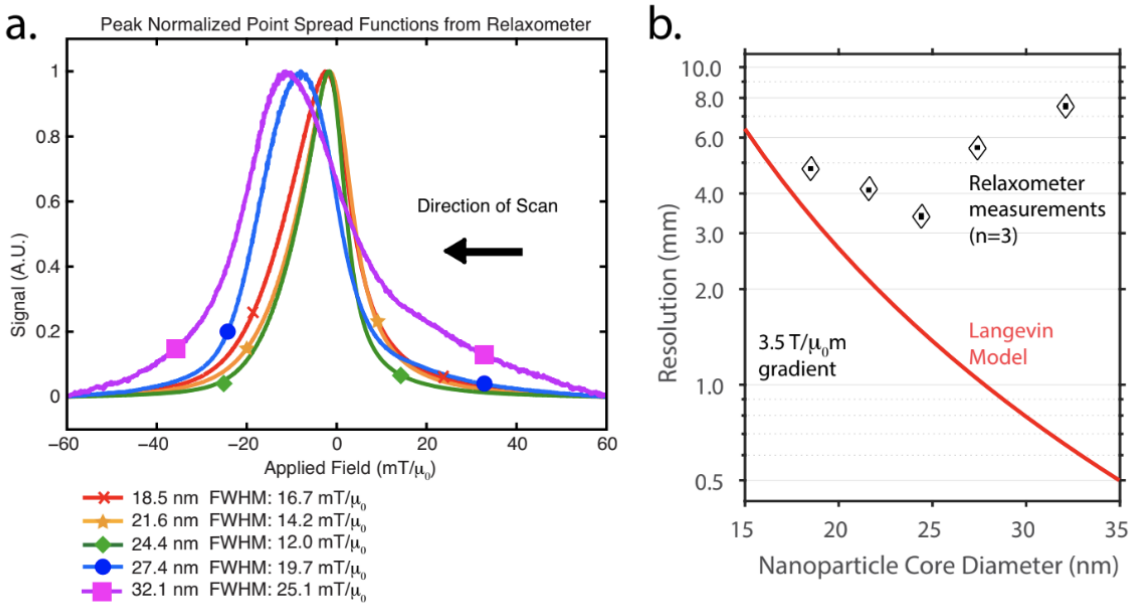

Figure 3.4: (a) Experimental 1D PSFs of Imagion Biosystems Precision MRX© SPIOs. The particle resolution increases as the core size increases until an upper limit is reached, at 24 nm. From that point on, relaxation is presumed to dominate, and the resolution decreases. (b) Comparison of experimentally measured particle resolution versus theoretically predicted. Republished with permission of IOP Publishing, Ltd, [64]; permission conveyed through Copyright Clearance Center, Inc.

inductance). Sinusoidal excitation leads to harmonics that represent the nanoparticle signal's spectrum. The first harmonic of the nanoparticle signal, however, is completely contaminated by direct feedthrough and hence it must be discarded. The direct feedthrough is almost 8 orders of magnitude stronger than the particle signal at the first harmonic and so the direct feedthrough filter must be very high order [93]. An arbitrary x-space excitation waveform for MPI is very challenging in part because the direct feedthrough interference would no longer be conveniently located at a single fundamental frequency. Hence, there would be no simple direct feedthrough filter.

To permit arbitrary excitation of magnetic nanoparticles, Tay et al. [92] developed what we call an arbitrary waveform relaxometer (AWR), as seen in Fig. 3.5. The AWR does not employ a direct feedthrough filter; instead, it uses a transmit receive coil pair, designed to fine tune the mutual coupling between transmit and receive coils. Tay at al. used a transmit-receive gradiometer with a real-time mechanical shimming adjustment. The receive coil is wound with two solenoids wound anti-series to minimize coupling to the uniform transmit coil. The sample is placed into only one of the receive coils, allowing subtraction of the

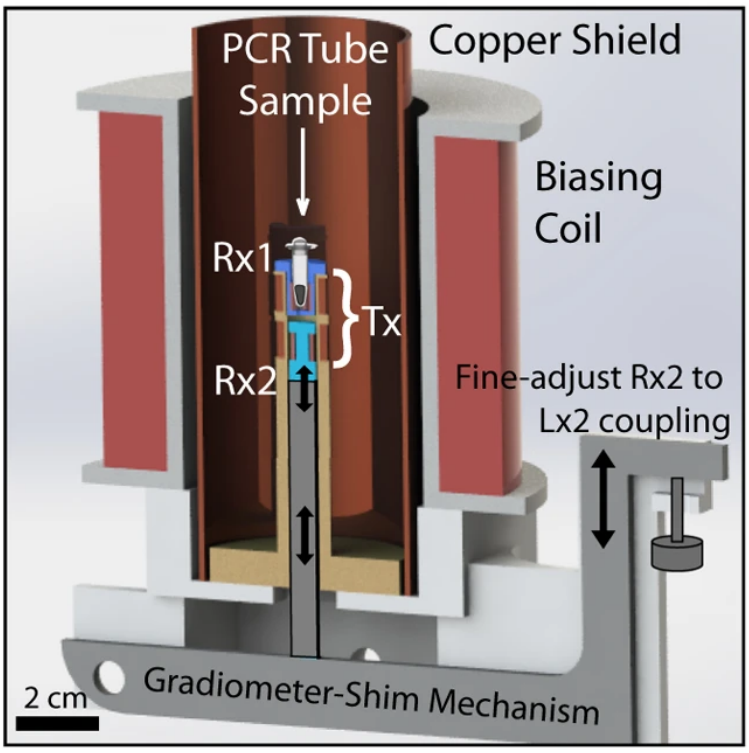

Figure 3.5: University of California, Berkeley's Arbitrary Waveform Relaxometer. Reproduced with permission of [92] under the Creative Commons Attribution (CC BY-NC) License (https://creativecommons.org/licenses/by-nc/4.0/).

transmit signal harmonic to occur without removing any nanoparticle signal. This device improved on prior work [94–96], and the fine mechanical shimming provided up to 67 dB cancellation, which allowed direct feedthrough to be smaller than the SPIO signals.

3.3.2.2 Transmit Amplitude and Sinusoidal Frequency

The Relaxation Wall hinders MPI spatial resolution from reaching its full potential [64]. We will show that the flexibility of the AWR allows us to obviate the relaxation wall using both Low-Amplitude, High Frequency (LAHF) MPI and Pulsed MPI [66, 67]. Both use non-conventional pulse sequences to probe the magnetization of samples. This section focuses on LAHF, which uses high-frequency and low-amplitude sinusoids.

Previous work has found that drive field amplitude and drive field frequencies affect the resolution and relaxation blur of an MPI PSF [65, 68, 97, 98]. Croft, et al. [65] showed that the spatial resolution for the blur from relaxation is linearly proportional to the transmit field frequency and the transmit field amplitude. It was found that MPI spatial resolution

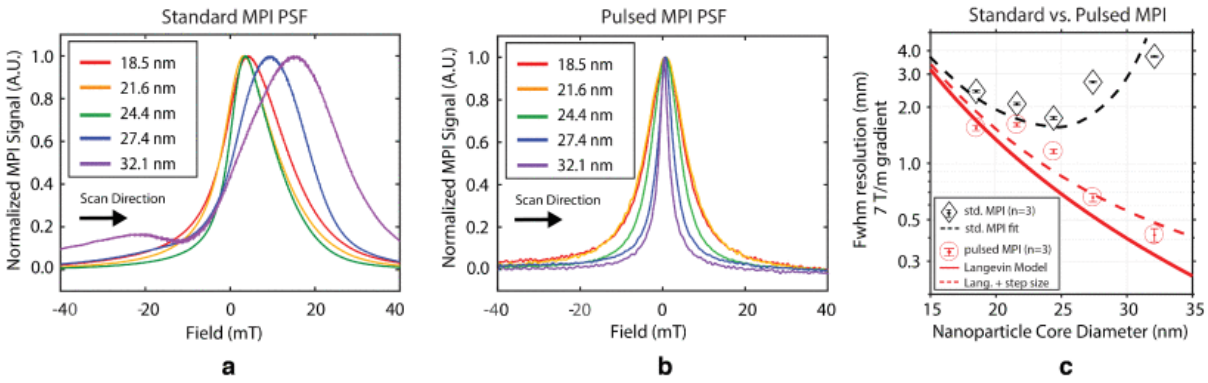

Figure 3.6: Experimental 1D comparison between conventional sinusoidal MPI at 25 kHz, 20 mT with square waved pulsed MPI at 2.5 kHz, 1 mT. (a) Standard sinusoidal pulse sequences make MPI PSFs widen after core sizes of 24 nm are reached due to relaxation effects. (b) Pulsed MPI for same nanoparticles shows constant improvement as a function of core size (c) Experimental sinusoidal excitation does not reach Langevin predictions with inflection point around 24 nm core size nanoparticle. Pulsed MPI reaches Langevin predictions. ©2019 IEEE. Reprinted, with permission, from [66].

generally improves with lower drive amplitudes and lower drive frequencies [65, 68], but MPI sensitivity improves with higher drive amplitudes and frequencies [99].

The relationship between resolution and transmit amplitude and frequency has been proven experimentally. Work by Tay, et al. [67] has explored this concept in detail, optimizing both the resolution and the SNR of particles based on these equations. They ultimately found that low drive amplitudes and low frequencies greatly improved the resolution of SPIOs at the cost of significant SNR.

However, low-amplitude and low-frequency MPI means that the sample is barely probed. Tay, et al. [67] found that the most optimal for SPIO resolution and SNR was to use low-amplitude, high-frequency drive waveforms. They called this drive waveform LAHF. The use of high frequencies compensates for the sensitivity loss of low amplitude drive waveforms.

3.3.2.3 Pulsed Magnetic Particle Imaging

Pulsed MPI was developed to mitigate relaxation effects in MPI images [66]. The relaxation wall has debilitating effects on MPI images, with relaxation limiting the minimum resolution that can be achieved by single-core nanoparticles. Pulsed MPI data acquisition was developed to overcome this [66]. Pulsed MPI is a scanning strategy that does not permit relaxation to blur the signal from one pixel to adjacent pixels. The idea is to allow relaxation dynamics to occur while the FFR is static. Pulsed MPI allows for image reconstruction without relaxation blurring, as seen in Fig. 3.6. However, Pulsed MPI cannot obviate SNR loss

of slow relaxation, especially at low amplitude drive fields. Importantly, Pulsed MPI has no direct feedthrough interference problem because the direct feedthrough occurs only during the transmit coil ramping. This is similar to the transmit and receive temporal decoupling in MRI.

This work has been experimentally proven, as shown in Fig. 3.6. Previous work saw that, because of relaxation, MPI PSFs significantly widen with sinusoidal excitation. Square wave MPI data follows the theoretical Langevin curve: asymptomatically approaching the theoretical Langevin resolution. For the largest tracer tested (32 nm core), pulsed MPI gave a spatial resolution of 450 μm in a 7 T/m scanner. For sinusoidal pulse sequences, that spatial resolution was 4 mm. Fig. 3.6 shows that pulsed MPI overcomes the relaxation wall.

3.4 Conclusions

In this chapter, I discussed MPI's search for improved spatial resolution, e.g., Pulsed MPI and larger SPIOs. Improving MPI's spatial resolution will enable its clinical translation. However, our survey concludes that the field has exhausted traditional Langevin physics to improve MPI's spatial resolution to a clinically competitive level. In the next chapter, we will examine new tracers that improve the resolution and sensitivity of MPI by 10x. This phenomenon is called superferromagnetism.

Chapter 4

Interacting Nanoparticles in Magnetic Particle Imaging

In this chapter, I first show experimental evidence of the improvements wrought by SFMIOs in MPI. Next, I describe the development of theoretical models and experiments that posit superparamagnetic chains are responsible for the 6-17x improvement in SNR and 5-13x resolution observed in superferromagnetic particles. The 1D chain formation model I introduce predicts the relationship between nanoparticle parameters and chain formation. My resulting work in 4 experiments support the model for the transition from superparamagnetism to superferromagnetism. Finally, I describe our conclusions for the experiments and how the experimental results inform future SFMIO work.

4.1 Introduction

Magnetic Particle Imaging (MPI) is a radiation-free, non-invasive imaging modality developed by Gleich and Weizenecker [1]. MPI is a distinct modality from Magnetic Resonance Imaging (MRI) and requires a special-purpose hardware scanner. MPI images the saturation properties of superparamagnetic iron oxide nanoparticles (SPIOs). MRI images the precession of the water proton's nuclear moments [8]. SPIOs are sometimes employed as a T1 or T2* contrast agent in MRI. In MPI, we detect the nonlinear signature (e.g., harmonics) from a flip of SPIOs. Importantly, there are zero harmonics from surrounding human or mammalian tissue, meaning MPI has superb contrast-to-noise ratio (CNR). The MPI signal is perfectly linear with the amount of iron within a voxel [4–6]. The electronic magnetization of SPIOs is 22 million times greater than the nuclear magnetization of ^{1}H at 7T, so MPI scanners can measure even 5 nanograms of iron per voxel (roughly 200 cells) [6, 8]. Finally, because typical MPI scans use drive fields with frequencies in the very low frequency (VLF) regime ($\sim$20 kHz) [2], there is no signal attenuation with depth inside an animal or human. Depth attenuation is a challenge for many imaging methods, including optical, ultrasound, and nuclear medicine. MPI's unique physics make it an ideal tracer imaging method with

applications in angiography, cell tracking, and perfusion imaging [12, 23, 36, 70, 100–104].

Philips [105] and a few labs have attempted to scale up MPI from pre-clinical to the much bigger bore size for human scanners necessary for clinical imaging [69, 106]. The main challenges include cost and human safety constraints (dB/dt and SAR) [2, 8] of whole-body gradient fields and drive fields necessary for high-resolution MPI [57, 107]. Gradient costs scale quadratically with gradient strength. A pre-clinical MPI murine scanner using ferucarbotran nanoparticles has a spatial resolution of 1.5 mm using a 7 T/m gradient with a 4 cm bore radius [6, 12]. Hence, a human-sized MPI scanner operating with a 1.0 T/m gradient using ferucarbotran would offer roughly 11.0 mm spatial resolution, which is not competitive with MRI (1 mm), CT (1 mm) or Nuclear Medicine ($\sim$ 3 – 5 mm). While deconvolution approaches could boost this resolution somewhat, it is clear we need a higher resolution MPI tracer for human applications.

The resolution in an MPI image is a complex research topic to be sure, but the undeconvolved resolution using X-space reconstruction is simply the ratio of the magnetic resolution of the nanoparticle to the gradient strength [57, 107]. All MPI scans today use superparamagnetic iron oxide nanoparticles (SPIOs) as the tracer. An ensemble of SPIOs show no remanence, meaning there is no net magnetization observed when the applied magnetic field is zero. Because the SPIOs are too far apart to interact at the concentrations employed in MPI, they respond only to the applied magnetic fields. This is the "non-interacting" assumption. Here we explore the advantages and tradeoffs of interacting SPIOs, which we call superferromagnetic tracers.

The steepness of a nanoparticle's M-H curve is responsible for the magnetic resolution measured. If the applied magnetic field flips from positive to negative magnetization, so does the SPIO's magnetization. The flip creates a change in magnetization which is inductively sensed, allowing the change in magnetization to create a pulse in the received signal. The speed of the flip and the width of the pulse in the received signal depend on physical properties of the nanoparticles. The main physical property that affects the speed of the flip is nanoparticle size. Previous work to optimize SPIO size and magnetic properties have only focused on individual nanoparticles, not assemblies [86, 108].

Recent work by Tay, et al. [109] has shown that assemblies of chain-like SPIOs, or superferromagnetic iron oxide nanoparticles (SFMIOs) can cause order-of-magnitude enhancement of both resolution and sensitivity, as seen in Fig. 4.1. SFMIOs are iron oxide nanoparticles that would be superparamagnetic if they weren't interacting with one another [110–112]. Superferromagnetic nanoparticles flip from negative to positive saturation much faster than superparamagnetic nanoparticles. In addition to the applied magnetic field, the superferromagnetic nanoparticles are affected by one another's induced magnetizations, enabling a faster flipping.

In this work, we show experimental data that supports the hypothesis that inter-particle interactions and formation of chains is responsible for the marked improvement in MPI resolution and sensitivity seen with SFMIOs. We find that SFMIO behavior depends on the following conditions: local concentration, solvent viscosity, transmit amplitude, and the length of time they are exposed to a magnetic field. Understanding the physics of how SFMIO

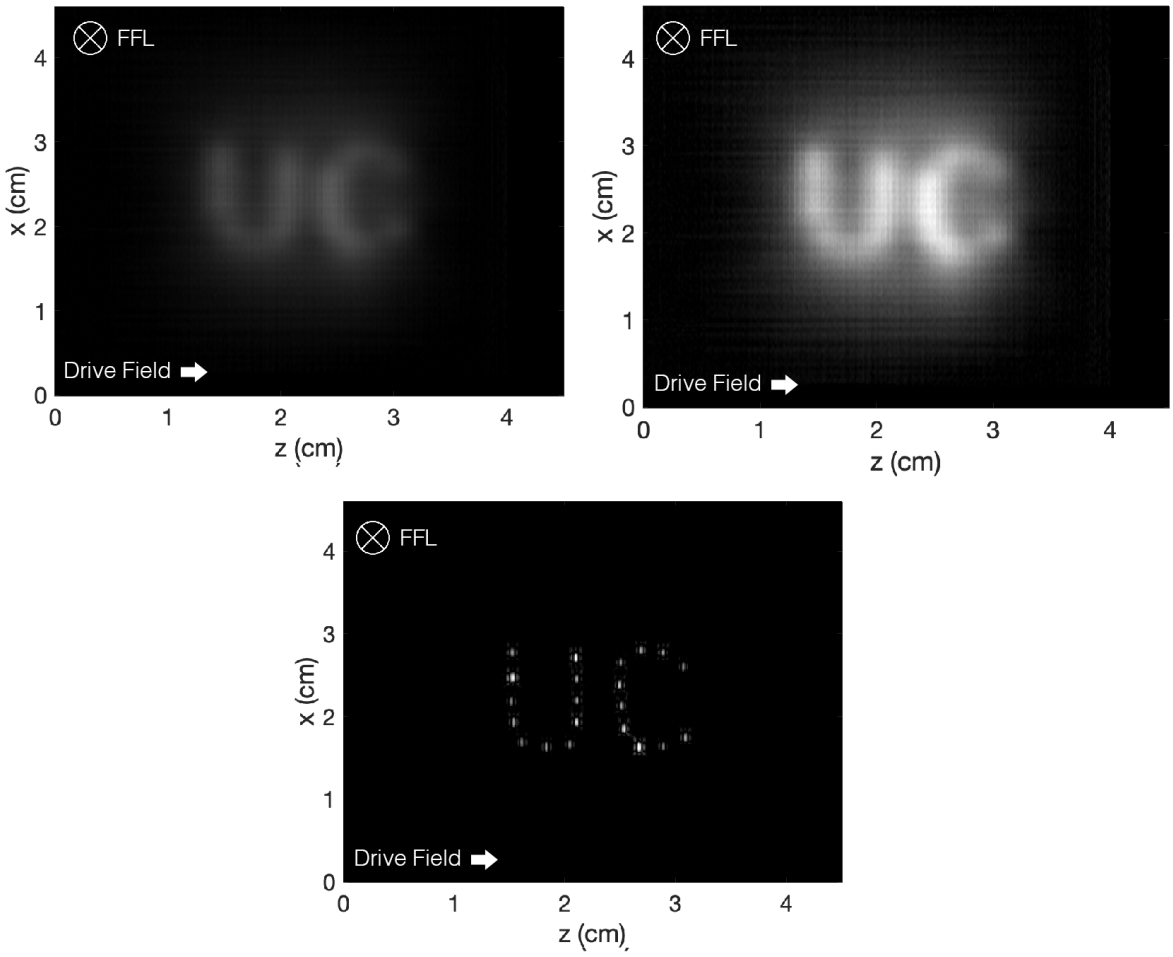

Figure 4.1: MPI Images of a UC phantom, which employed 300-micron diameter holes filled with SFMIO or Vivotrax tracers, spaced 2.35 mm apart. The two phantoms were scanned with identical MPI parameters. These scans took place on a custom-built vertical bore 2D Projection MPI Scanner with a 6.3 T/m gradient field. Both SPIOs and SFMIOs underwent the exact same pulse sequence. Nanoparticles were excited at a transmit frequency of 20.225 kHz and a transmit amplitude of 40 mTpp. The scanning phantom was mechanically translated in the z-direction at 0.5mm increments. The FOV was 4.5 cm by 4.6 cm, with a scan time of 5 min. The images at the top show SPIOs (Vivotrax), and the bottom image shows SFMIO tracers synthesized by our lab. The top left image is SNR normalized, then multiplied by 2.5 so that it would be more visible. The top right figure and the bottom figure are both peak normalized. The measured spatial resolution (FWHM) in a 6.3 T/m gradient was $\approx$ 1.5 mm for SPIOs vs 300 μm for SFMIOs. This demonstrates SFMIOs can improve resolution by 5-fold and offer a 17-fold boost in SNR.

behavior is induced is essential for determining biocompatible encapsulation properties and one of the ways pulse sequences need to be adjusted for SFMIO behavior to occur.

4.2 Theory

In this section, I review the theory that SPIO chain formation is responsible for the 5-13x improvement in resolution and 6-17x improvement in SNR. I first explain the Langevin saturator model, which models the magnetization of an ensemble of nanoparticles that begin to experience magnetic attraction to one another. I then go over the 1D chain formation model, a simple model that inspired our subsequent experiments on the conditions for optimal chain formation. This models the magnetomotive force between two nanoparticles which experience magnetic attraction.

4.2.1 X-space Magnetic Particle Imaging with Superparamagnetic Iron Oxide Nanoparticles

MPI measures the magnetization of superparamagnetic iron oxide nanoparticles in response to an applied magnetic field, which, in a 1D X-space model, is proportional to the Langevin function. Because these particles are superparamagnetic and their magnetic moments instantaneously align with an applied field, a changing applied magnetic field creates changing magnetization of the nanoparticles. The changing magnetization is measured inductively, so MPI's 1D point spread function is proportional to the derivative of the Langevin Function.

The spatial resolution (FWHM) of the MPI equation depends only on the strength of G, the Gradient field $[T/m]$, and the magnetic properties of the nanoparticles themselves, k $[m/A]$, where, for a single domain magnetic nanoparticle, $k = \frac{\mu_o}{k_B T}\frac{M_{sat}\pi}{6d^3}$. The magnetic resolution of an MPI scan using traditional SPIO particles is inversely proportional to the strength of the gradient field and inversely proportional to the cube of the magnetic core diameter. Intuitively, one would keep increasing the magnetic core diameter of SPIOs to optimize MPI resolution [57, 107]. However, Tay et al. [64] found that, after the nanoparticles reached a certain magnetic core diameter, the magnetic relaxation of the particles started to dominate, leading to blurring in the MPI image. The larger the magnetic core of a superparamagnetic particle, the further away it is from the single-domain particle description that describes superparamagnetism.

The traditional Langevin physics used to describe superparamagnetic nanoparticles has a few assumptions that must be met to accurately predict behavior. 1) A superparamagnetic particle must be small enough to be a single magnetic domain. 2) When the applied magnetic field is zero, the net magnetization of the nanoparticles should also be zero. 3) The magnetization of an SPIO is described by the Langevin Function. The advantage in using superparamagnetic nanoparticles for MPI is both in their 'instantaneous' flip from negative to positive saturation and in their nonlinear magnetic saturation.

4.2.2 Interacting Superparamagnetic Nanoparticles

Recent work by Tay, et al. [109], showed that new superferromagnetic tracers improve the resolution and sensitivity of MPI by more than 10-fold. These particles show ferromagnetic behaviors such as coercivity and remanence, but the switch from positive to negative saturation is much steeper than superparamagnetic nanoparticles. Fig. 4.4 demonstrates this by showing an M-H curve similar to ferromagnetic materials, showing hysteresis that is not seen in superparamagnetic materials. It also shows that the nanoparticles with these properties form chains under applied fields. Tay, et al. [109] found that those chained particles meet the definition of superferromagnetism. They found that magnetization of superferromagnetism could be modeled as a Langevin Saturator, a transcendental equation where the output magnetism builds upon the induced magnetism of neighboring SPIOs.

$$M(t) = L\left(\frac{H_{tx}(t) + \alpha\beta M(t)}{H_{sat}}\right) \tag{4.1}$$

where H_{tx} is the applied magnetic field, H_{sat} is $\frac{1}{kG}$, M is the magnetization of the chaining nanoparticles, and β is a dimensionless parameter that describes the saturation magnetization of the chain. α is another dimensionless parameter that describes how closely the nanoparticles in a chain can be packed. Any applied magnetic field to change the chain's magnetization direction must overcome the magnetic field produced by each nanoparticle's neighbor. This models the hysteresis, coercivity, and remanence as seen in the superferromagnetic samples.

This function also alludes to the process of chain formation because $M(t)$ increases in magnitude as the particles draw closer to one another. Assuming that the conditions of potential aggregation of nanoparticles are met, the equation begins with a nanoparticle feeling the magnetic field of its neighboring nanoparticle. As the neighboring nanoparticle drifts closer, β increases, leading the nanoparticle's magnetization to increase, increasing the draw of the neighboring nanoparticle, and so on.

4.2.2.1 1D Chain Formation

The hypothesis of chaining nanoparticles naturally brings new predictions as a consequence. Almost all previous works of MPI assumes that SPIOs are non-interacting. These nanoparticle assemblies found by Tay et al. [109] hypothesize that superferromagnetic behavior is caused by the formation of chains of SPIOs. If this is true, then I hypothesize these four corollaries.

1. If nanoparticles are below a certain concentration, no superferromagnetic behavior should be observed.
2. The formation of chains should depend on the viscosity of the solvent that the particles are in, even for Néelian nanoparticles.
3. Superferromagnetic behavior should be observed after time exposed to magnetic field, called the polarization time.

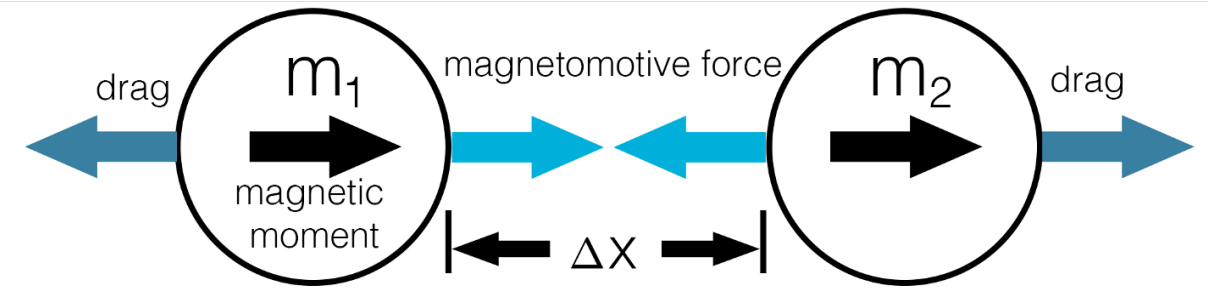

Figure 4.2: 1 dimensional free body diagram of two nanoparticles affected by one another's induced magnetic field. As their magnetic moments align with the spatially constant applied magnetic field, an attractive magnetic field is induced in each nanoparticle. This induced magnetic field does vary spatially, and therefore, it produces a magnetomotive force. 1D Stoke's drag resists the magnetomotive force that draws the two nanoparticles together.

4. If particles are not polarized past some threshold, presumably the coercive threshold, then superferromagnetic behavior should not be observed.

If these predictions are true, the case for chain formation of SPIOs being responsible for superferromagnetic behavior is much stronger.

It is essential to understand the conditions that lead to the observed experimental results of chain formation. To this end, we developed a 1D model that finds how chain formation time scales with viscous drag, particle size, and initial concentration. This is a simple model that has been derived before, but we found it particularly useful for understanding the chain formation process [113].

In this model, each superparamagnetic nanoparticle has aligned with a constant applied magnetic field. If each particle is close enough to feel the other's induced dipole moment, then a magnetomotive force is formed, drawing them closer together. The Stoke's drag of the viscous surrounding fluid resists the motion. With typical SPIOS, the Stoke's drag on each particle is enough to dominate its induced magnetomotive force.

$$\nabla_x(m \cdot B) = 6\pi\eta b\Delta\dot{x} + qE \tag{4.2}$$

This equation solves for the time it takes for the distance between the two nanoparticles to go to zero, where m is the magnetic moment of the particles, q is the electric charge of the particles, η is solvent viscosity, and b is the hydrodynamic radius of the two particles. In the case of our experimental results, the nanoparticles are in a non-polar solvent and thus have no surface charge. Therefore, the electric field term can be disregarded, leading to a simple solution for the distance between the two nanoparticles as a function of time

$$\Delta x(t) = \sqrt[1/5]{x_0^5 - 5\frac{\gamma}{\Omega}t} \tag{4.3}$$

where x_0 is the initial distance between the particles, and the analogue to concentration, γ is $3\mu_0 m^2/\pi$, where m is the magnetic moment of the particles. Ω is $12\pi\eta b$. The solution to equation 4.3 indicates that the chain formation time, which is the time it takes for particles to attract one another, depends most strongly on the concentration of the particles in solution. There should also be a dependence on viscosity: the more viscous the solution, the longer it takes for chains to form.

4.3 Materials and Methods

In this section, I discuss the process to undertake these experiments. First, I cover how we synthesize the SFMIOs. I then go into how the SFMIOs were characterized by iron concentration assays and TEM. Finally, I review the unique pulse sequence designed for this experiment on the lab's arbitrary waveform relaxometer.

4.3.0.1 SFMIO Synthesis

Prior work detailed and experimentally confirmed the process of creating single-core magnetite nanoparticles [80]. This method had two steps: first, the creation of an iron-oleate precursor, and second, the thermal decomposition of the precursor to form magnetic nanoparticles. The synthesis procedure is as follows: first, a stoichiometric amount of iron acetylacetonate and oleic acid (3.3 g and 15 mL, respectively) were placed in a reaction flask with stirring at a rate of 300 rpm. The flask was then placed in a molten solder bath at a temperature of 290° C. The temperature of the bath was then raised to 320° C. 30 min after being placed in the bath, the flask was removed and allowed to come to room temperature. The next day, the prepared iron-oleate precursor was used to synthesize the magnetic nanoparticles. First, the precursor, at 0.62 M, was diluted with 1-octadecene to create a 0.22 M mixture. The diluted mixture was then loaded into a syringe. It was then dripped into a reaction flask containing 5.1 mL of octadecene for 25 minutes. The solder bath was stabilized at 360° C and the sample within the reaction flask was stirred vigorously at a rate of 300 RPM. After cooling overnight, the resulting mixture was then washed in hexane in a 1:1 mixture, then centrifuged at 14 kRCF for 30 min. The resulting supernatant was discarded and only the precipitated particles were saved. This process was repeated multiple times.

4.3.0.2 Nanoparticle Characterization

The precise mass of iron in the SFMIO sample was determined using Perls' Prussian blue reaction as described in [114]. In this process, 40 μl of SFMIOs were first digested in 1 mL of 12M HCl. After digestion, the resulting solution was mixed with 100 μl of 5% potassium ferrocyanide. Absorbance was measured in a UV-Vis Spectrophotometer at two wavelengths, 680 nm and 730 nm. The absorbance of the SFMIOs was then compared to a calibration curve made through the same process that used SPIOs of a known concentration

of ferucarbotran (Vivotrax). TEM images of chained SPIOs were made by placing 3 μl samples on formvar-coated copper grids that then dried under static 22 mT applied fields for 5 h. The chains were then confirmed by transmission electron microscopy (JEOL 1200EX, 80 kV). For the viscosity experiments, the solvent viscosity was determined by referring to [115]. In this paper, proportional mixtures of hexane and squalane were created and their material properties measured. We first dried SFMIO samples in hexane. We then resuspended the samples in mixtures of hexane and squalane. We then performed a nonlinear least squares fit [115] on the data and back calculated the resulting viscosity of our samples. This gave us an estimate of the solvent viscosity.

4.3.0.3 Resolution and Sensitivity Calculation

Spatial Resolution is calculated, using the Houston Criterion, from the Full Width Half Maximum (FWHM) of the image of a point source, which is often called the Point Source Function or PSF. Resolution in MPI is converted from a magnetic resolution (mT) to a spatial resolution (mm) by dividing the result by the 3D scanner's gradient field strength (T/m). The Berkeley 3-D MPI Scanner has a gradient of 7 T/m, leading to 1 mT becoming a spatial resolution of 140 μm. MPI Signal strength (mV/mg Fe) was calculated by dividing the voltage of the received signal by the iron mass of the tracer. That number is then normalized by the concentration-normalized MPI signal measurement of Vivotrax.

4.3.1 Pulse Sequence to measure Chain Formation

The SFMIOs were tested on our arbitrary waveform relaxometer (AWR), as described by prior work from the lab [92]. The AWR's non-resonant coil design enables the creation of custom pulse sequences, hence, arbitrary. The AWR can reconstruct the magnetization response such that a 1D point-spread function (PSF) that characterizes the entire sample within the device. The chain formation was measured using a unique pulse sequence designed to quantify the change in PSF as a function of the length of time a prepolarizing pulse was applied to the sample. The pulse sequence is repeated 1 ms long prepolarizing pulses (TP) followed by 20 kHz (TR) readouts. This sequence (prepolarizing pulse + readout) was repeated continuously for a total sequence length of 1.4 s.

4.4 Discussion and Results

In this section, I first demonstrate the change in SFMIO PSF as a function of time exposed to an applied prepolarizing field with a comparison of Ferucarbotran's response. I also show how the SPIO to SFMIO transition is affected by amplitude of the applied field. I then show that the measured PSF can be linearly decomposed as a transition between a population of SPIOs to a population of chained SPIOs, aka SFMIOs. The following two sections show that the transition from SPIO to SFMIO is affected by both the concentration of the nanoparticles within the sample and the viscosity of the solvent the nanoparticles are in.

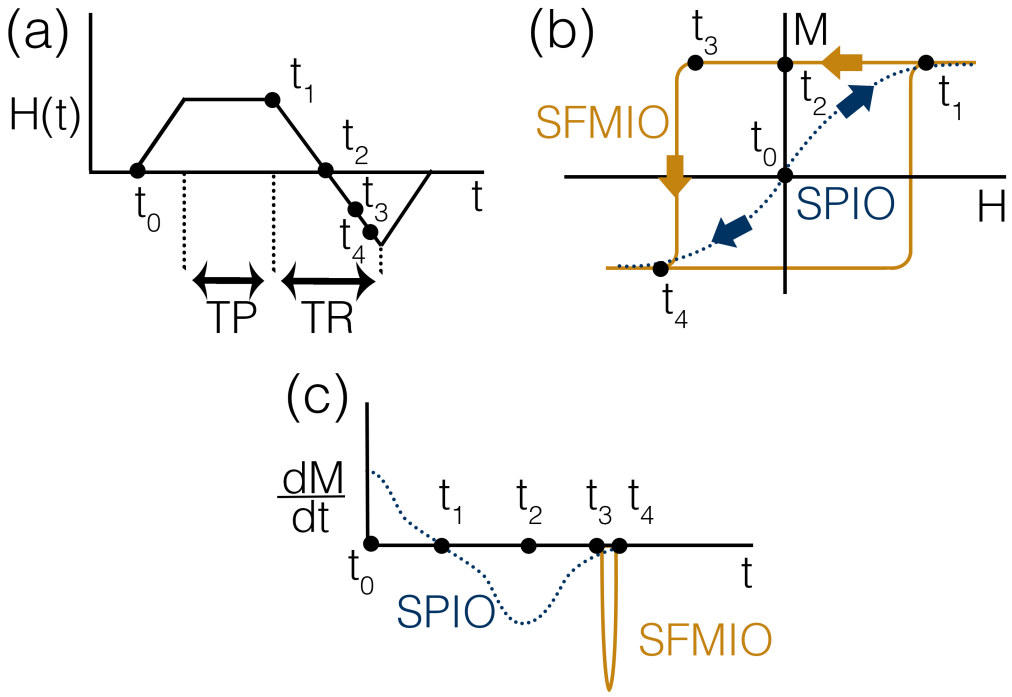

Figure 4.3: This pulse sequence allows us to uniquely observe the chain formation time with excellent SNR. (a) Chain Formation Pulse Sequence. From t_0 to t_1, the AWR is ramped up to a constant applied field and a prepolarizing pulse is applied, the length of which is TP. t_1 to t_4 shows the readout time, TR, which describes the length of time the applied field goes from maximum to minimum amplitude. (b) M-H curve showing SPIO and SFMIO magnetization as a function of applied field. If the sample shows SPIO behavior, the SPIO magnetization curve is followed. If the sample shows SFMIO behavior, the SFMIO magnetization curve is followed. c) $\dot{M}$(t) plot showing the inverse of what the receive coil measures. From t_0 to t_1, an SPIO PSF is seen. No SFMIOs have been formed yet. If no chains are formed after TP, SPIO behavior will be seen during TR, t_1 to t_4. If chains do form during TP, TR will show SFMIO behavior, where the steep change in magnetization change from t_3 to t_4 in (b) is responsible for a sharp resolution and increase in SNR seen in (c).

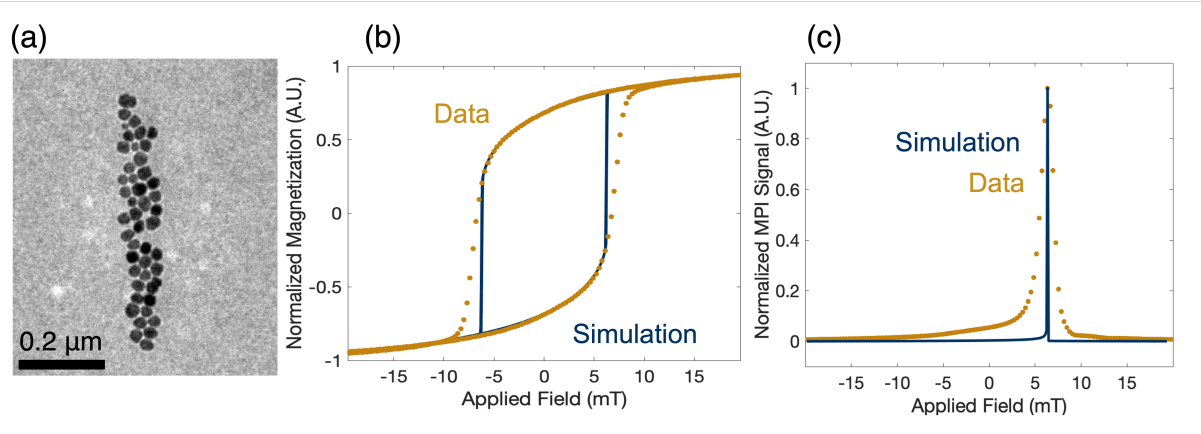

Figure 4.4: Chaining Hypothesis Experimental Data and Theoretical Predictions (a) TEM Images of Chain Formation in SFMIO samples. SFMIO samples were exposed to 16 mT magnetic fields. Samples distinctly show chain formation in the direction of the applied field. (b) Experimental data and Theoretical Predictions of SFMIO M-H curves. The SFMIO curve shows both coercivity and remanence characteristic of ferromagnetic materials. Its behavior is correctly modeled by a Langevin "saturator" element as detailed in [109]. (c) Theoretical Predictions and Experimental data of SFMIO PSFs. There is strong agreement between the theoretical predictions and the experimental data.

4.4.1 Langevin Saturator Theoretical Prediction of Experimental Data

The Langevin saturator model in Eq. 4.1 predicts step-like transitions from positive to negative saturation or vice versa. It also predicts coercivity and remanence, much like a ferromagnet. Fig. 4.4 shows experimental data and theoretical modeling of the SFMIO M-H curve. These predictions were experimentally verified, showing that SFMIO behavior is accurately modeled by the Langevin saturator model. Deviations from the predicted behavior during the process of transitioning from one saturation to another are thought to be due to coercivity dispersion.

4.4.2 Transition from SPIO to SFMIO behavior as a function of applied field Duration

Our results in Figs. 4.5 and 4.6 clearly show the difference in SFMIO PSF properties as a function of prepolarization time. In Fig. 4.5, the change is shown in 3 PSFs at different prepolarizing times. The most dramatic change in resolution occurs within 25 ms of exposure to a prepolarizing field. This fast change in transition is supported by Fig. 4.6, where the transition in both resolution and peak signal of an SFMIO sample occurs within the first

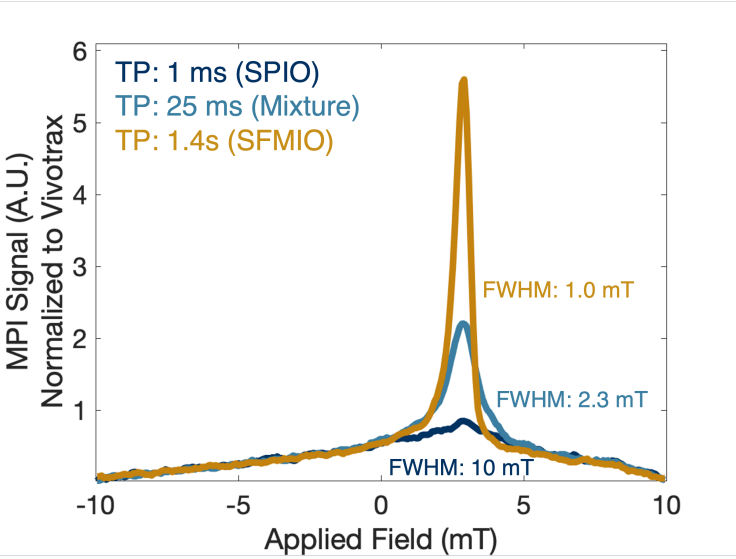

Figure 4.5: PSF of SFMIO sample as a function of prepolarization time. As the amount of time the sample is exposed to an applied magnetic field increases, the MPI signal and magnetic resolution improves accordingly. The PSF at a prepolarization time of 1ms demonstrates SPIO behavior. The PSF at a prepolarization time of 25 ms shows a 5x improvement in resolution and a 2x increase in MPI signal. We consider the PSF at 25ms to show a mixture of SPIO and SFMIO behavior. After 1.4 s have passed the MPI signal has increased by 6-fold and has a 2-fold improvement in resolution. This PSF shows fully SFMIO behavior, with a total 6-7x increase in MPI signal and a 10x improvement in magnetic resolution.

50 ms. By 1.4 s of prepolarizing time, the final PSF has a resolution of 1 mT and a 6-7x increase in peak signal. This leads to a total improvement in resolution by 10x and an 6-7x increase in signal strength. In contrast, Ferucarbotran, undergoing the same pulse sequence, stayed constant in both resolution and peak signal.

This change in particle resolution and peak signal as a function of time exposed to an applied field affects MPI pulse sequences by indicating that, for a very short amount of time, each sample should be polarized into chain formation before implementation of a pulse sequence. Because the time that the polarization takes for most samples is within the millisecond range, this should not be a difficult requirement to meet.

4.4.3 Transmit field amplitude threshold of SFMIO signal

Fig. 4.7 provides additional support to the Langevin saturator model by confirming the role of transmit field amplitude in the chain formation process. When the transmit amplitude is below this threshold (2 mT), no SFMIO behavior is seen. Fig. 4.3 shows that, unless the some transmit amplitude threshold is reached, only an SPIO response is seen. However,

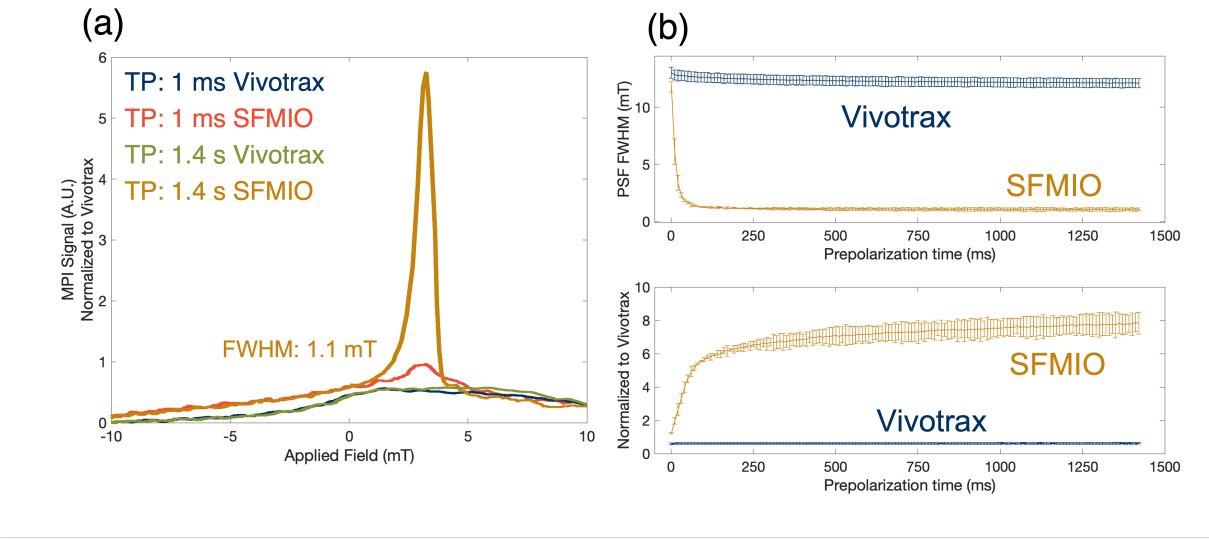

Figure 4.6: Change in MPI PSF and MPI signal as a function of prepolarization time (TP). (a) The SFMIO PSF from a 1ms TP to a 1.4 s TP shows a complete change in magnetic resolution as compared to the Vivotrax PSF. (b) The SFMIO sample undergoes a 10x improvement (11.8 mT to 1.1 mT) in magnetic resolution as a function of TP. The Vivotrax sample stays constant in the same pulse sequence with a magnetic resolution of 12.5 mT. The SFMIO MPI signal undergoes a 7x increase as a function of TP while the Vivotrax MPI signal stays constant.

when the transmit amplitude was greater than that threshold (12 mT), SFMIO behavior was seen.

The existence of a threshold for SFMIO behavior means that transmit amplitude must be greater than either a sample's coercivity or saturation field (H_{sat}). We would need nanoparticles where H_{sat} is smaller than the coercive threshold of the chain to test the mechanism for the threshold thoroughly. We currently have only synthesized particles that have a coercivity threshold less than H_{sat}. The threshold observed is most likely a coercivity threshold.

We found experimentally that each "batch" of SFMIOs synthesized has different coercive behaviors. While this is the case, it is possible that each SFMIO batch needs to be characterized before its use in MPI pulse sequences. However, SFMIO synthesis is still very much in early stages. There is room for improvement in the synthesis process.

4.4.4 Linear Decomposition of Signal

Analysis of the PSF change as a function of prepolarization time as seen in Fig. 4.5 shows that transition from SPIO to fully chained SFMIOs does not occur immediately and goes

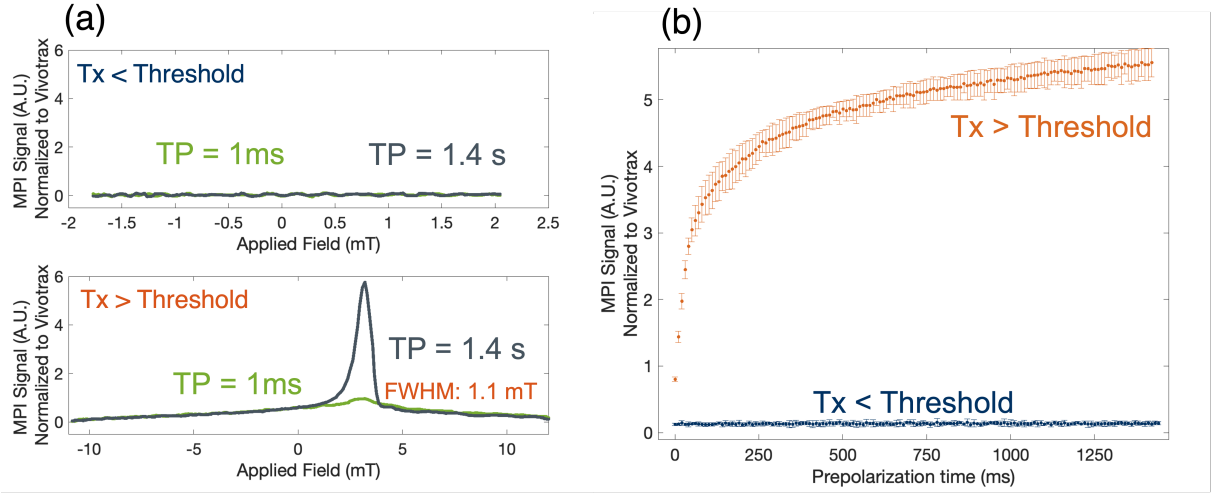

Figure 4.7: In this experiment, the pulse sequence shown in Fig. 4.3 is repeated. However, the transmit amplitude of the applied field is varied in two different cases, one above the applied field threshold as shown in Fig. 4.3 (b), and one below the applied field threshold. The chaining hypothesis indicates that SFMIOs will only "flip" and show SFMIO behavior if the transmitted magnetic field is above the particle's coercivity threshold. This plot shows that to be a possibility, where a transmitted field of 2 mT shows an MPI signal of less than 1, while a transmitted field of 12 mT shows the expected SFMIO behavior, a reduction of 10x resolution and an increase in MPI signal.

through transition phases. Intuitively, this seems very reasonable. Each TP and TR are repeated, with a total scan length of 1.4 s. From the first TR to the last TR, the amount of iron nanoparticles within the sample stays constant. The SPIOs chain as they are exposed to prepolarizing pulses. This chaining occurs over some period of time. Therefore, it is reasonable to say that there are two populations of particles within the sample, chained and unchained.

In this analysis, we make three assumptions. The first is that the very first PSF, barely exposed to the prepolarizing pulse, shows completely SPIO behavior and has no chained SPIOs. The second assumption is that the final PSF that has been exposed to 1.4 s of prepolarizing time shows completely SFMIO behavior and has negligible free-floating SPIOs giving signal. The third assumption we make is that, in the sample, the nanoparticles can either be free-floating or chained. We then showed in Fig. 4.8 that we can linearly decompose the results of our pulse sequence into two populations - free or chained particles. Note that the point where the SFMIO signal begins to dominate aligns with Fig. 4.6's change in resolution and peak signal.

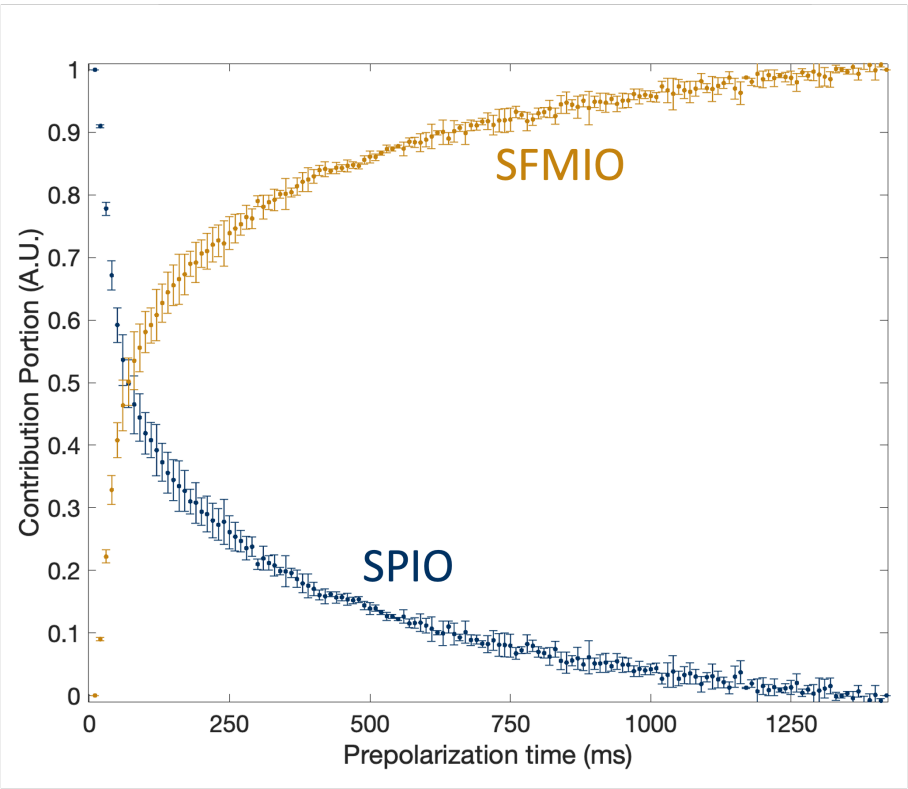

Figure 4.8: Linear decomposition of sample transition from fully SPIO to fully SFMIO behavior. This shows the transition from 'free' floating SPIOs to chained SPIOs, aka SFMIOs. Note that the transition from SPIO to SFMIO domination occurs at the same time as Fig. 4.6's noticeable change in Peak Signal and resolution. This is from the same data set.

4.4.5 Concentration and Solvent Visocity dependence of Chain Formation Time

Eq. 4.3 indicates that the time it takes for SPIOs to form chains will depend on the concentration of iron in the sample and the viscosity of the solvent the nanoparticles are in. The initial interparticle distance, x_0, relates to the initial concentration by $(\frac{1}{x_0})^3$. x_0 then has a fifth root relationship with the chain formation time. Fig. 4.9 shows how even a modest change in concentration (as seen in the bottom plot) dramatically boosts the magnetic resolution if the concentration permits chain formation. For example, a 3x reduction in concentration (from 2.7 to 0.7 mV/mg Fe) leads to virtually no change in the resolution, but another drop of 0.3 mg/ml, almost completely turns "off" any SFMIO behavior. Tay, et al. [109], hypothesized that biocompatible encapsulation, much like micelles, should be used to enforce a high local concentration of SFMIOs and a low systemic concentration for biosafety. These concentration results show that threshold concentrations must be exceeded

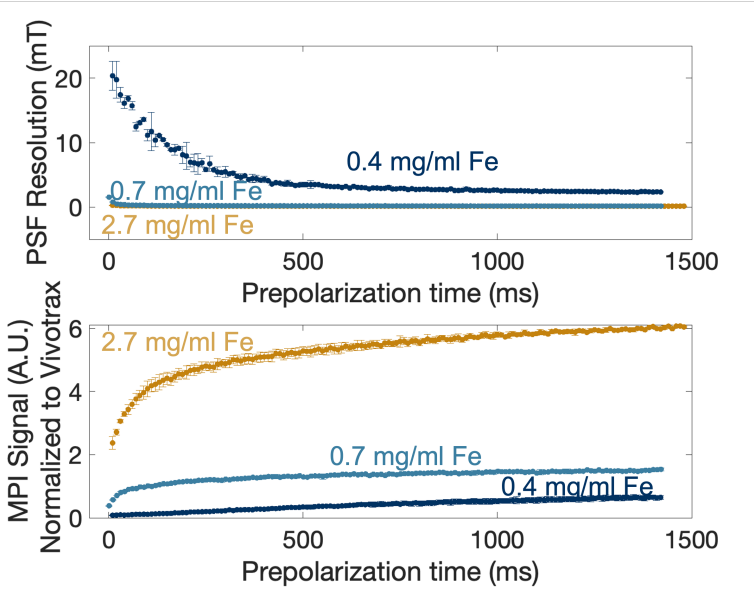

Figure 4.9: Change in SPIO to SFMIO transition as a function of particle concentration. In the top plot, a small change in behavior occurs between 2.7 mg/ml Fe and 0.7 mg/ml Fe. However, a very large change in SFMIO behavior occurs with a 0.3 mg/ml difference in sample concentration, with the 0.4 mg/ml sample showing a much less steep transition between the first magnetic resolution measurement and the last. The bottom plot demonstrates that the peak signal of each sample is affected by the concentration of the particles, with the lowest concentration showing very little change in peak signal as a function of prepolarization time at all. Note that while the 0.7 mg/ml sample shows very little change in magnetic resolution from the 2.7 mg/ml sample, its peak signal is 5x lower in SNR. This is, presumably, from the reduction of iron in the sample.

such that SFMIO behavior is still seen within biocompatible encapsulation.

Fig. 4.10 shows how the change in solvent viscosity affects SFMIO behavior. Solvent viscosity has a crucial effect on the SFMIO behavior; if the fluid viscosity is too high, then Stoke's drag will dominate the magnetomotive force and hence chain formation will occur very slowly. In the 1D Chain formation model, the solvent viscosity should have a fifth root relationship with the chain formation time. We saw that as solvent viscosity increased, the chain formation time increased. Note that the final resolution of each sample was also worse. This underlines how important it will be to ensure low viscosity fluid inside biocompatible encapsulations.

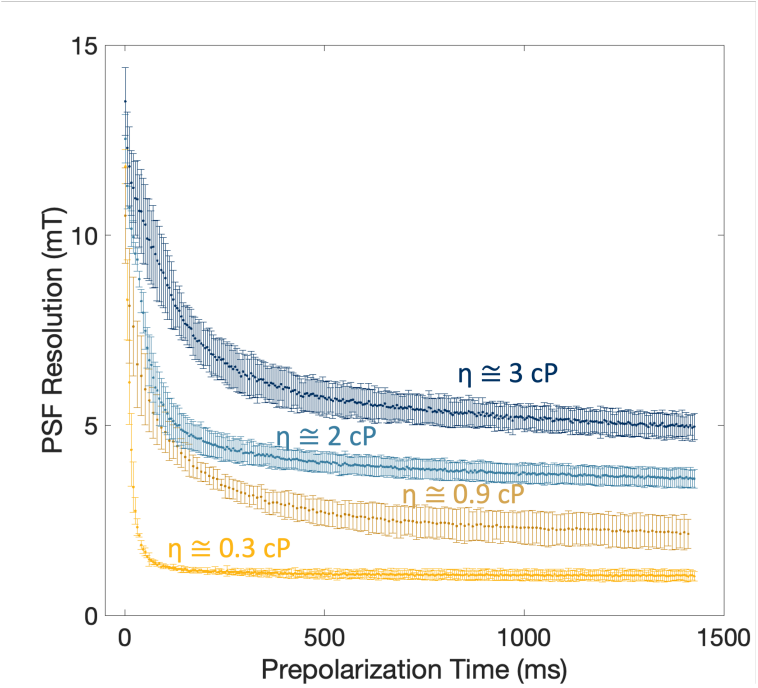

Figure 4.10: Plot of PSF magnetic resolution vs. prepolarization time for various viscosities. The change in resolution from SPIO to SFMIO behavior seems to occur around the same time, which is not predicted by the chain formation model. Note that the final magnetic resolution of each sample lowers as the solvent viscosity increases. There does not seem to be any further decrease in magnetic resolution as a function of prepolarization time.

4.5 Conclusion

In conclusion, we have demonstrated that SFMIO behavior does not occur immediately and that a transition between SPIO and SFMIO behavior occurs as a function of exposure to magnetic fields. This result supports previous work that showed that chains of superparamagnetic nanoparticles were responsible for order-of-magnitude improvement in MPI sensitivity and resolution.

MPI is a promising pre-clinical *in vivo* imaging modality. It has many strengths, e.g., no signal depth dependence, linear positive contrast, non-radioactivity. However, to this point, its clinical implementation has been held back by its poor resolution in small animal scanners. Superferromagnetic iron oxide nanoparticles are a new tracer for use in MPI that alleviate this resolution issue by 10x, along with an increase in sensitivity.

These results in this chapter will inform future work on biocompatible encapsulations for SFMIOs and pulse sequence design. Pulse sequences must have transmit amplitudes that exceed the transmit amplitude threshold of the sample SFMIOs. Pulse sequences must also

include short periods of time for chains to fully polarize. The biocompatible encapsulation for the particles themselves must have concentrations within that are high enough to see SFMIO behavior, and the solvents inside the biocompatible encapsulation must be as low viscosity as possible. These conditions will help enable SFMIOs to be successfully used in MPI scans.

Chapter 5

Future Work

The search for improved resolution in MPI has circumvented the limitations of Langevin physics. This was spurred by the development of new tracers: superferromagnetic nanoparticles. Their use in MPI will produce highly sensitive, high-resolution scans. However, with every new advance comes new challenges and possibilities for applications. This chapter reviews such potentials.

5.1 SFMIO Challenges

In this section, I will discuss challenges posed by the use of SFMIOs in MPI. These challenges include safety concerns, questions of biocompatibility, and the need for novel pulse sequence design. Superferromagnetic nanoparticles have extraordinary promise *in vitro*, but face problems to become successful *in vivo* tracers. This section discusses how such challenges to clinical translation may be overcome.

5.1.1 Magnetomotive Force and Biocompatible Encapsulation Design

Superferromagnetism in MPI raises new concerns about the adverse effects of magnetomotive force in scans. SPIO chains have the potential to assemble into structures that can move when exposed to large external magnetic fields. Appropriate caution must be taken to address this. This issue informs the design of biocompatible encapsulation to create safe tracers for superferromagnetic MPI.

To understand the design requirements for safe biocompatible encapsulation, we must first understand the nature of the magnetomotive force problem. The 1D Chain Formation model elucidates greater understanding of the problem. As discussed in Section 4.2.2, there are two forces operating in the 1D Chain formation model: magnetomotive force and Stoke's drag. Here the equation

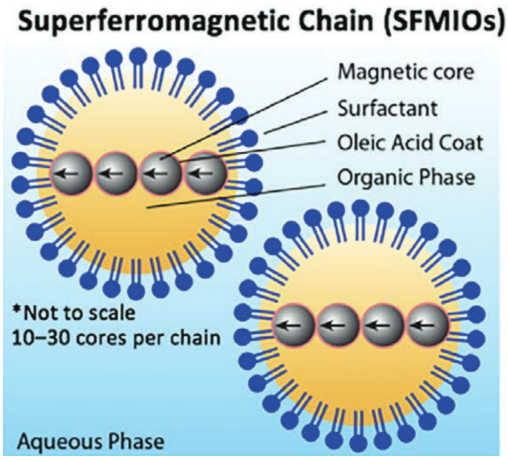

Figure 5.1: Schematic of the SFMIO nanoparticle encapsulation design. Illustration is not-to-scale, and there are ≥30 magnetic cores per SFMIO chain. Reprinted with permission from [109]. ©Wiley 2021.

$$F = \nabla_x (m \cdot B) \tag{5.1}$$

represents the force, F, on a magnetic moment, m, in an external magnetic field B. F denotes the rate of change of the total mechanical momentum of the system [116]. Stoke's drag is the other operating force in the 1D Chain Formation model. It describes the viscous drag on a sphere [117] and is shown by the equation:

$$F = 6\pi\eta b\dot{\vec{x}} \tag{5.2}$$

where F is the drag force, η is the viscosity of the solvent the sphere is in, and b is the hydrodynamic radius of the sphere. The interaction of these forces in the 1D chain formation model has implications about the safety of magnetomotive forces operating within the body.

With typical SPIO nanoparticles, the magnetomotive force is much less than the drag force. Consider a magnetite nanoparticle with a 20 nm magnetic core diameter, with a typical magnetic dipole moment 10^{-19} or 10^{-18} $(A \cdot m^2)$ [118]. The distance between that particle and its neighbor is 200 nm. This makes the maximum inter-particle force 37.5 fN. The force produced by that particle and its neighbors is much less than the typical Brownian force that Stoke's drag represents, around 0.01 pN [119]. Therefore, Stoke's drag dominates any magnetomotive forces produced by a single nanoparticle.

Chained nanoparticles, however, have very different physics from independently acting nanoparticles. Imagine that N nanoparticles are aligned in a chain. The volume of that chain increases by N, one for every nanoparticle in the chain. This chain is then aligned with a magnetic field and moves along the path of the magnetic field. While drag resists this movement, it is only dependent on the hydrodynamic radius of a single nanoparticle,

not the volume of the chain. The force acting against the movement of the chain will remain constant, regardless of the length of the chain. In a chain with ten thousand nanoparticles, the magnetomotive force produced by that chain is much greater than any Brownian drag resisting that motion. This chain of nanoparticles would move in a magnetic field. This thought experiment illuminates a significant safety hazard with the use of superferromagnetic tracers in MPI.

In the seminal paper on superferromagnetism in MPI, Tay et al. [109] postulates that the issue of magnetomotive force could be mitigated by novel forms of biocompatible encapsulation. Much like a micelle, its purpose would be to maintain a high local concentration and a low systemic concentration. The encapsulation would help alleviate concerns with magnetomotive force by limiting the number of nanoparticles that could be chained within the capsule. The larger surface area of a micelle would also dissipate the force by increasing the surface area available for Brownian drag. This encapsulation would be 1 μm in size for vascular and cell labeling applications.

However, such encapsulation has not yet been successfully implemented. There are challenges to encapsulating the SFMIOs while retaining their high-resolution nature. One challenge is determining the number of particles within the encapsulation. Simulations performed by Chinmoy Saayuja, a graduate student in my lab, indicate that SFMIO behavior should occur even with just two nanoparticles.

5.1.2 Magnetic Fluid Heating and Pulse Sequence Design

Specific absorption rate (SAR) is another critical factor to consider with the use of SFMIOs in MPI. Superferromagnetic nanoparticles have M-H curves that resemble ferromagnets with hysteresis, coercivity, and remanence. This creates an area within the M-H curve that is equal to the energy dissipated per cycle per unit volume. This leads to magnetic fluid heating and hyperthermia.

Traditional MPI pulse sequences with SFMIOs could exacerbate SAR. Current MPI scans raster what is called small partial FOVs (pFOV) where the pFOV is defined by the transmit amplitude of the applied field. These pFOVs tile to an entire FOV. This pFOV pulse sequence trajectory includes a large amount of overlap due to reconstruction requirements in X-space reconstruction. Each pFOV is a full cycle that dissipates heat. Depending on the number of pFOVs in a scan, a single pulse sequence could produce large amounts of unnecessary heating.

SAR produced by SFMIOs is proportional to the frequency of the transmit field applied to the particles. The energy dissipated per cycle due to hysteresis can be estimated as follows:

$$P_{hyst} \approx 4\mu_0 M_{sat} H_c f \tag{5.3}$$

where M_{sat} is the saturation magnetization of the sample, H_c is its coercivity, f is the frequency of excitation of the sample, and μ_0 is the permeability of free space. Intuitively,

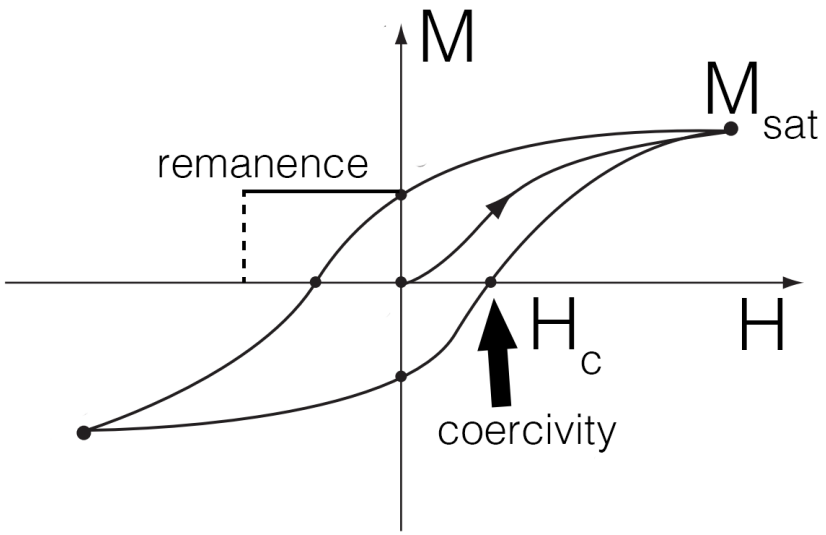

Figure 5.2: Hysteresis of a Ferromagnet and Superferromagnet. H_c is the coercive threshold for the magnet, the value of magnetic field for a "flip" from one saturation state to another to occur. M_{sat} is its saturation magnetization, the maximum magnetization a sample can produce, no matter what magnetic field is applied.

the higher the frequency of the applied field, the higher the amount of heat dissipated. For superferromagnetic MPI to succeed, novel pulse sequences must be developed to ensure patient safety.

My lab colleagues have developed a safe, potentially FDA approvable pulse sequence for SFMIOs [109, 120]. This pulse sequence is called the "Single Pass and Raster" (SPaR) sequence. Unlike traditional MPI pulse sequences, it covers the entire FOV at once, rather than just pFOVs. This reduces the number of cycles dissipated per raster of the FOV, thereby reducing the amount of heating produced. This work also demonstrates that SFMIO resolution and SNR/pg Fe depend on the frequency of excitation. SFMIO behavior is still shown at a lower frequency than the typical 20kHz used for MPI excitation. This is another avenue to reduce the hysteric power dissipated and create a safe pulse sequence for SFMIOs in MPI.

5.2 SFMIO Future Work

SFMIOs offer enormous advantages for MPI. They improve both MPI's resolution and sensitivity by an order of magnitude. SFMIOs will enable the translation of MPI to clinical settings. In this section, I will discuss future work with studying SFMIO physics, the poten-

tial for human sized MPI scanners, and its potential for vascular imaging and cell tracking. These questions and applications are worth pursuing in the future.

5.2.1 Chain Formation and SFMIO physics

Understanding SFMIO physics to make the best tracer possible is essential for their implementation in MPI. In this dissertation, I explored how transmit field amplitude, concentration, and viscosity affect the process of chain formation. However, there is more work to be done in studying SFMIO physics in greater detail. These unknown questions affect scientific understanding, scanning trajectories, and SFMIO synthesis procedures.

Two significant questions about SFMIO physics are:

- What relaxation mechanism (Brownian or Néelian) is responsible for the "flip" from one magnetic saturation to another?
- Does the chain turn physically to align with applied magnetic fields in different directions? Or does it break apart and reform?

Even studying the chain formation model itself, we did not get the opportunity to study how nanoparticle magnetic core volume affects the process of chain formation. These are just a few of many questions about the physics of SFMIOs.

5.2.2 Clinical Human Scanners

Clinical human scanners are essential for the future of MPI. An ideal clinical MPI scanner will have the following traits: affordability, minimal motion artifacts, water cooled magnets, and a resolution of 1 mm per voxel. SFMIOs *in vivo* would make these possibilities reality. Fig. 5.3 shows a comparison in magnetic fields between a 1 T/m gradient MPI scanner and a 0.2 T MRI scanner. This figure shows the affordability of an MPI clinical scanner with SFMIOs.

5.2.3 Cell Tracking

MPI excels at cell tracking in small animal scanners. Scaling up to human sized scanners opens opportunities for clinical MPI, for the first time. MPI could address a significant problem assessing cell-based therapies: an inability to directly monitor treatments [121]. One of the most interesting applications, currently, is immunotherapies, especially CAR-T (chimeric antigen receptor) cell therapies.

Adoptive cell therapies, including CAR-T, have had impressive successes in treating cancers such as melanoma, cervical cancer, and leukemia [122]. These therapies are designed to interface with a patient's individual biomarkers to target their cancer specifically [122]. They could target antigens on cancer surfaces without any off-target damage to healthy tissues. This is literally personalized medicine.

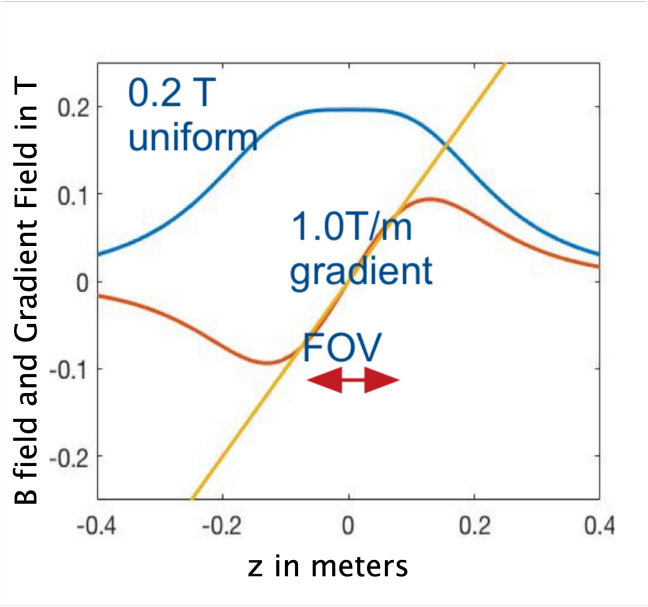

Figure 5.3: The blue line shows the magnetic field for a 0.2 T/m MRI scanner. The orange line shows the same FOV but with a 1 T/m gradient used in MPI. Both have the same bore diameter of 40 cm. The cost of a 1 T/m gradient MPI scanner would be the same as a 0.2 T MRI scanner.

These therapies have extraordinary promise but have difficulties in evaluating their efficacy. Currently, evaluating cancer symptoms with metabolic markers such as FDG PET is the checkpoint that determines treatment efficacy [123]. However, this can take weeks from time of treatment. Tracking cells to tumors could evaluate treatments in a matter of days. SFMIOs in MPI could offer long-term, stable, monitoring of the distribution of cells used in CAR-T cell therapy.

5.2.4 Vascular Imaging

MPI with SFMIOs has great potential in the field of vascular imaging. One possible application is that of stroke imaging. Currently, stroke imaging is typically done with three completely different X-ray and CT scans [124–126]. The first X-ray is to differentiate ischemic versus hemorrhagic strokes. If that stroke is not hemorrhagic, then a second CT scan is performed using angiography. A third CT scan is performed to evaluate tissue perfusion. MPI has the possibility of changing stroke care because all three of these evaluating scans could be done with a single MPI scanner, or even, scan.

However, the most important benefit that SFMIOs in MPI has in stroke imaging is improving its already excellent CNR. SFMIOs will allow for the first time, clear assessment of capillary level perfusion. Previous work has been done to implement stroke imaging

in MPI; SFMIOs could improve those attempts to be clinically feasible. MPI has been used in cerebral blood volume and cerebral blood flow scans [102, 127], but lacked detailed resolution for perfusion scans; a successful scan only differentiated a healthy from an ischemic hemisphere of the brain. SFMIOs could be used to determine perfusion of the brain in detail.

Chapter 6

Conclusions

MPI's search for improved spatial resolution has spanned novel scanner, tracer, and pulse sequence design. However, it has become clear that MPI has reached the limitations of Langevin physics without achieving a spatial resolution competitive with other clinically used modalities such as CT and MRI. The introduction of superferromagnetism has injected new life into the search for improved spatial resolution. Superferromagnetic nanoparticles improve the resolution and sensitivity of MPI by 10-20x.

This work's contribution to the field of MPI is providing the first experimental demonstration of nanoscale superferromagnetic physics in MPI. It was shown from my work that chain formation of SPIOs depends on the following parameters:

- **Prepolarization Time** I found that SFMIO behavior was induced from seemingly superparamagnetic nanoparticle behavior under the influence of a magnetic field. In optimal conditions, SFMIOs improve the resolution and sensitivity an order of magnitude. This change in behavior typically occurred within 50 ms or less. Understanding chain formation time is essential for pulse sequence design. A short prepolarizing magnetic field at the beginning of a pulse sequence would ensure SFMIO behavior throughout an MPI scan.

- **Amplitude of polarizing magnetic field** Choosing transmit amplitudes above the either the coercive threshold or H_sat is essential for SFMIO pulse sequences. My work highlighted that SFMIO behavior was only induced when transmit amplitudes were above a threshold. SFMIO behavior did not occur in samples that had transmit amplitudes below that threshold.

- **Concentration of SFMIO sample** I found the induction of SFMIO behavior had nonlinear changes dependent on a sample's concentration. This work is important for determining minimum concentration in biocompatible encapsulation for SFMIO imaging.

- **Viscosity of SFMIO solvent** I demonstrated that SFMIO behavior is dependent on the viscosity of the solvent that the SFMIO is suspended in. This work shows that the low viscosity solvents are necessary for ideal SFMIO behavior.

The use of superferromagnetic nanoparticles in MPI is a challenge that requires a new understanding of MPI physics. However, this challenge is worthy because SFMIOs bring a 10-20x improvement in resolution and sensitivity: a necessary goal of MPI for at least the past 10 years. This work has extended the understanding of superferromagnetic behavior in MPI and the best conditions for its behavior. Understanding the physics of SFMIO particles will enable clinical MPI. It could also revolutionize MPI's two main applications, cell tracking and vascular imaging. An improved understanding of SFMIO behavior will help motivate future developments and uses of MPI.

Appendix A

Derivation of Chain Formation Model

This models the electrostatic force and the magnetomotive force between two superparamagnetic nanoparticles in a magnetic field. In this model, the two superparamagnetic nanoparticles are already aligned with the magnetic field.

$$\begin{aligned} P_1 : \mu_1 \ddot{\vec{x}}_1 &= \nabla_x (m_1 \cdot B_2) - 6\pi\eta b_1 \dot{\vec{x}}_1 - q_1 E_2 \\ P_2 : \mu_2 \ddot{\vec{x}}_2 &= -\nabla_x (m_2 \cdot B_1) + 6\pi\eta b_2 \dot{\vec{x}}_2 + q_2 E_1 \end{aligned} \tag{A.1}$$

In these equations, m is the magnetic moment of the particles, B is their induced magnetic fields, b is their hydrodynamic radius, η is the viscosity of the solvent surrounding them, q is their charge, and E is their electric fields.

Note: typically, the electromagnetic force is characterized with the Lorentz force equation:

$$F_e = q(\vec{E} + \vec{v} \times \vec{B}) \tag{A.2}$$

However, in this case, the velocity of the nanoparticles is in the same direction as the applied magnetic field, thus rendering the second half of the equation zero. In the case that this field is no longer strictly within a single direction, the second half of this equation must be considered.

$$\begin{aligned} E(\vec{x}) &= \frac{q}{4\pi\epsilon_0} \frac{\hat{x}}{|\vec{x} - \vec{x}_m|^2} \\ E(x) &= \frac{q}{4\pi\epsilon_0} \frac{1}{|x - x_m|^2} \end{aligned} \tag{A.3}$$

$$\begin{aligned} B(\vec{x}) &= \frac{\mu_0}{4\pi} \frac{3\hat{n}(\hat{n} \cdot \vec{m}) - \vec{m}}{|\vec{x} - \vec{x}_m|^3} \\ B(x) &= \frac{\mu_0}{2\pi} \frac{m}{|x - x_m|^3} \end{aligned} \tag{A.4}$$

$$\begin{aligned} \mu_1 &= \mu_2 \\ b_1 &= b_2 \\ m_1 &= m_2 \\ q_1 &= q_2 \end{aligned} \tag{A.5}$$

We assume that the two particles are identical. Because these are nanoparticles and their mass is insignificant, the inertial force in equation A.1 can be discarded.

$$\mu \approx 0 \tag{A.6}$$

One dimensional so all dot products become multiplication

$$\begin{aligned} \nabla_x(mB_2) - 6\pi\eta b\dot{x}_1 - qE_2 = 0 \\ -\nabla_x(mB_1) + 6\pi\eta b\dot{x}_2 + qE_1 = 0 \end{aligned} \tag{A.7}$$

Setting equations equal to one another

$$m\nabla_x(B_1 + B_2) - 6\pi\eta b(\dot{x}_1 + \dot{x}_2) - q(E_1 + E_2) = 0 \tag{A.8}$$

Plugging in equations for B_1, B_2, E_1, E_2

$$\frac{\mu_0 m^2}{2\pi}\nabla_x\left(\frac{1}{|x_2 - x_1|^3} + \frac{1}{|x_1 - x_2|^3}\right) - 6\pi\eta b(\dot{x}_1 + \dot{x}_2) - \frac{q^2}{4\pi\epsilon_0}\left(\frac{1}{|x_2 - x_1|^2} + \frac{1}{|x_1 - x_2|^2}\right) = 0 \tag{A.9}$$

Define

$$|x_2 - x_1| = |x_1 - x_2| = x \tag{A.10}$$

We then define the first derivative of x

$$\frac{d}{dt}(|x_2 - x_1|) = \frac{d}{dt}(|x_2 - x_1|) \tag{A.11}$$

We then use the following definition

$$\begin{aligned} \frac{d}{dt}(|\vec{u}|) &= \dot{\vec{u}}\frac{\vec{u}}{|\vec{u}|}, u \neq 0 \\ &= \dot{\vec{u}}\hat{u}, u \neq 0 \end{aligned} \tag{A.12}$$

Because we've already decided that because it's 1D we'll get rid of the unit vector.

We then define the first derivative of x

$$\begin{aligned} \frac{d}{dt}(|x_2 - x_1|) = \frac{d}{dt}(|x_2 - x_1|) &= \dot{x} \\ \dot{x_2} - \dot{x_1} = \dot{x_1} - \dot{x_2} &= \dot{x} \\ \dot{x_1} = \dot{x_2} &= \dot{x} \end{aligned} \tag{A.13}$$

Therefore

$$\frac{-3\mu_0 m^2}{\pi}\left(\frac{1}{x^4}\right) - \frac{q^2}{2\pi\epsilon_0}\left(\frac{1}{x^2}\right) = 12\pi\eta b\dot{x} \tag{A.14}$$

We now define the following substitutions:

$$\begin{aligned} \Omega &= 12\pi\eta b \\ \chi &= \frac{-q^2}{2\pi\epsilon_0} \\ \gamma &= \frac{-3\mu_0 m^2}{\pi} \\ \psi &= \frac{\gamma}{\chi} = \frac{3\mu_0}{2\epsilon_0}\left(\frac{mq}{\pi}\right)^2 \end{aligned} \tag{A.15}$$

$$\begin{aligned} \Omega\dot{x} &= \chi\frac{1}{x^2} + \gamma\frac{1}{x^4} \\ &= \frac{\chi x^2 + \gamma}{x^4} \\ \frac{1}{\Omega} &= \frac{x^4}{\chi x^2 + \gamma}\dot{x} \\ \frac{1}{\Omega\chi} &= \frac{x^4}{x^2 + \psi}\dot{x} \end{aligned} \tag{A.16}$$

$$\begin{aligned} \int \frac{x^4}{x^2 + \psi}\frac{dx}{dt}dt &= \int \frac{1}{\Omega\chi}dt \\ \int \frac{x^4}{x^2 + \psi}dx &= \int \frac{1}{\Omega\chi}dt \end{aligned} \tag{A.17}$$

We then do long division such that

$$\frac{x^4}{x^2 + \psi} = x^2 - \psi + \frac{\psi^2}{x^2 + \psi} \tag{A.18}$$

Our equation then becomes

$$\int x^2 dx - \int \psi dx + \int \frac{\psi^2}{x^2 + \psi}dx = \int \frac{1}{\Omega\chi}dt \tag{A.19}$$

With the initial conditions such that

$$t(x = x_0) = 0 \tag{A.20}$$

The solution for equation A.19 is

$$\chi\Omega\left[\frac{1}{3}\left(|x^3 - x_0^3|\right) - \psi(|x - x_0|) + \psi^{\frac{3}{2}}\left(arctan\left(\frac{\sqrt{\psi}(|x - x_0|)}{\psi + x_0 x}\right)\right)\right] = t(x) \tag{A.21}$$

In the case where the two particles are as close to another as can be:

$$t(x = 0) = \chi\Omega[\frac{x_o^3}{3} - \psi x_o + \psi^{\frac{3}{2}} arctan(\frac{x_o}{\sqrt{\psi}})] \tag{A.22}$$

In the case that there is no surface charge and $q = 0$, equation A.14 becomes:

$$\frac{-3\mu_0 m^2}{\pi}\left(\frac{1}{x^4}\right) = 12\pi\eta b\dot{x} \tag{A.23}$$

Solving it in a similar fashion as equation A.14 gives us

$$\int x^4 dx = \int \frac{\gamma}{\Omega} dt \tag{A.24}$$

With the same initial conditions as equation A.20, we get a result such that

$$x(t) =^{1/5} \sqrt{x_0^5 - 5\frac{\gamma}{\Omega}t} \tag{A.25}$$

Note that in equation A.25 and in equation A.22, both solutions are true in the range $x0 \leqq x \leqq 0$. Both equations are zero outside of that range. An additional note: in equation A.25, we drew out the minus sign inherent of γ to better illustrate the nature of the solution.

Bibliography

[1] Bernhard Gleich and Jürgen Weizenecker. "Tomographic imaging using the nonlinear response of magnetic particles". In: *Nature* 435.7046 (June 2005), pp. 1214–1217. ISSN: 1476-4687. DOI: 10.1038/nature03808.

[2] Emine U. Saritas et al. "Magnetostimulation Limits in Magnetic Particle Imaging". In: *IEEE Transactions on Medical Imaging* 32.9 (2013), pp. 1600–1610. DOI: 10.1109/TMI.2013.2260764.

[3] Michelle L. James and Sanjiv S. Gambhir. "A Molecular Imaging Primer: Modalities, Imaging Agents, and Applications". In: *Physiological Reviews* 92.2 (2012), pp. 897–965. DOI: 10.1152/physrev.00049.2010.

[4] Kuan Lu et al. "Linearity and shift invariance for quantitative magnetic particle imaging". In: *IEEE transactions on medical imaging* 32.9 (Sept. 2013), pp. 1565–1575. ISSN: 1558-254X. DOI: 10.1109/TMI.2013.2257177.

[5] Bo Zheng et al. "Magnetic Particle Imaging tracks the long-term fate of in vivo neural cell implants with high image contrast". In: *Scientific Reports* 5.1 (Sept. 2015), p. 14055. DOI: 10.1038/srep14055.

[6] Bo Zheng et al. "Quantitative Magnetic Particle Imaging Monitors the Transplantation, Biodistribution, and Clearance of Stem Cells In Vivo". In: *Theranostics* 6 (2016), pp. 291–301. DOI: 10.7150/thno.13728.

[7] Christine Rümenapp, Bernhard Gleich, and Axel Haase. "Magnetic Nanoparticles in Magnetic Resonance Imaging and Diagnostics". In: *Pharmaceutical Research* 29.5 (May 2012), pp. 1165–1179. ISSN: 1573-904X. DOI: 10.1007/s11095-012-0711-y.

[8] Emine U. Saritas et al. "Magnetic particle imaging (MPI) for NMR and MRI researchers". In: *Journal of magnetic resonance (San Diego, Calif. : 1997)* 229 (Apr. 2013), pp. 116–126. ISSN: 1096-0856. DOI: 10.1016/j.jmr.2012.11.029.

[9] Min Lu et al. "FDA report: Ferumoxytol for intravenous iron therapy in adult patients with chronic kidney disease". In: *American Journal of Hematology* 85.5 (2010), pp. 315–319. DOI: https://doi.org/10.1002/ajh.21656.

[10] Harris Khan et al. "Safety and efficacy of a single total dose infusion (1020mg) of ferumoxytol". In: *Therapeutic Advances in Hematology* 12 (2021), p. 20406207211006022. DOI: 10.1177/20406207211006022.

[11] Charles H. Cunningham et al. "Positive contrast magnetic resonance imaging of cells labeled with magnetic nanoparticles". In: *Magnetic Resonance in Medicine* 53.5 (2005), pp. 999–1005. DOI: https://doi.org/10.1002/mrm.20477.

[12] Elaine Y. Yu et al. "Magnetic Particle Imaging: A Novel in Vivo Imaging Platform for Cancer Detection". In: *Nano Letters* 17.3 (Mar. 2017), pp. 1648–1654. DOI: 10.1021/acs.nanolett.6b04865.

[13] Hamed Arami et al. "Tomographic magnetic particle imaging of cancer targeted nanoparticles". In: *Nanoscale* 9 (47 2017), pp. 18723–18730.

[14] Yasuhiro Matsumura and Hiroshi Maeda. "A new concept for macromolecular therapeutics in cancer chemotherapy: mechanism of tumoritropic accumulation of proteins and the antitumor agent smancs". In: *Cancer research* 46.12_Part_1 (1986), pp. 6387–6392.

[15] Jun Wu. "The Enhanced Permeability and Retention (EPR) Effect: The Significance of the Concept and Methods to Enhance Its Application". eng. In: *Journal of personalized medicine* 11.8 (Aug. 2021), p. 771. ISSN: 2075-4426. DOI: 10.3390/jpm11080771.

[16] Arun K. Iyer et al. "Exploiting the enhanced permeability and retention effect for tumor targeting". In: *Drug Discovery Today* 11.17 (2006), pp. 812–818. ISSN: 1359-6446. DOI: https://doi.org/10.1016/j.drudis.2006.07.005.

[17] Stefan Wilhelm et al. "Analysis of nanoparticle delivery to tumours". In: *Nature Reviews Materials* 1.5 (Apr. 2016), p. 16014. DOI: 10.1038/natrevmats.2016.14.

[18] Qin Dai et al. "Quantifying the Ligand-Coated Nanoparticle Delivery to Cancer Cells in Solid Tumors". In: *ACS Nano* 12.8 (Aug. 2018), pp. 8423–8435. DOI: 10.1021/acsnano.8b03900.

[19] K. Ley. "Functions of selectins". In: *Results Probl Cell Differ* 33 (2001), pp. 177–200.

[20] Steven R Barthel et al. "Targeting selectins and selectin ligands in inflammation and cancer". In: *Expert Opinion on Therapeutic Targets* 11.11 (2007), pp. 1473–1491. DOI: 10.1517/14728222.11.11.1473.

[21] Alessandro Natoni, Matthew S. Macauley, and Michael E. O'Dwyer. "Targeting Selectins and Their Ligands in Cancer". In: *Frontiers in Oncology* 6 (2016). DOI: 10.3389/fonc.2016.00093.

[22] Sébastien Boutry et al. "Specific E-selectin targeting with a superparamagnetic MRI contrast agent". In: *Contrast Media & Molecular Imaging* 1.1 (2006), pp. 15–22.

[23] Katie M. Parkins et al. "Visualizing tumour self-homing with magnetic particle imaging". In: *Nanoscale* 13 (12 2021), pp. 6016–6023. DOI: 10.1039/D0NR07983A.

[24] K.L. Barry Fung et al. "Rapid in situ labelling and tracking of neutrophils and macrophages to inflammation using antibody-functionalized MPI tracers". In: *International Journal on Magnetic Particle Imaging* 8.1 ().

[25] Nicole B. Day, William C. Wixson, and C. Wyatt Shields. "Magnetic systems for cancer immunotherapy". In: *Acta Pharmaceutica Sinica B* 11.8 (2021), pp. 2172–2196. ISSN: 2211-3835. DOI: https://doi.org/10.1016/j.apsb.2021.03.023.

[26] Julia J. Gevaert et al. "Magnetic Particle Imaging is a sensitive in vivo imaging modality for the quantification of dendritic cell migration". In: *bioRxiv* (2021). DOI: 10.1101/2021.09.22.461401.

[27] Prashant Chandrasekharan et al. "Non-radioactive and sensitive tracking of neutrophils towards inflammation using antibody functionalized magnetic particle imaging tracers". In: *Nanotheranostics* 5.2 (Feb. 2021), pp. 240–255. DOI: 10.7150/ntno.50721.

[28] Gang Ren et al. "Abstract 2770: Imaging cancer immunology: Monitoring CD47 mAb treatment in vivo by magnetic particle imaging". In: *Cancer Research* 80.16 (Aug. 2020), pp. 2770–2770.

[29] James Mansfield et al. "Imaging cancer immunology: Systemic tracking of immune cells in vivo with magnetic particle imaging". In: *Journal of Nuclear Medicine* 61.supplement 1 (2020), pp. 101–101.

[30] Jeremy B. Swann and Mark J. Smyth. "Immune surveillance of tumors". In: *The Journal of clinical investigation* 117.5 (May 2007), pp. 1137–1146. DOI: 10.1172/JCI31405.

[31] Zebin Xiao and Ellen Puré. "Imaging of T-cell Responses in the Context of Cancer Immunotherapy". In: *Cancer Immunology Research* 9.5 (May 2021), pp. 490–502. ISSN: 2326-6066. DOI: 10.1158/2326-6066.CIR-20-0678.

[32] A. W. Segal et al. "Indium-111 Labeling of Leukocytes: A Detrimental Effect on Neutrophil and Lymphocyte Function and an Improved Method of Cell Labeling". In: *Journal of Nuclear Medicine* 19.11 (1978), pp. 1238–1244. ISSN: 0161-5505.

[33] David A. Goodwin. "Cell Labeling with Oxine Chelates of Radioactive Metal Ions: Techniques and Clinical Implications". In: *Journal of Nuclear Medicine* 19.5 (1978), pp. 557–559. ISSN: 0161-5505.

[34] Shinya Yamanaka. "Pluripotent Stem Cell-Based Cell Therapy—Promise and Challenges". In: *Cell Stem Cell* 27.4 (2020), pp. 523–531. DOI: https://doi.org/10.1016/j.stem.2020.09.014.

[35] Patricia K. Nguyen, Johannes Riegler, and Joseph C. Wu. "Stem Cell Imaging: From Bench to Bedside". In: *Cell Stem Cell* 14.4 (2014), pp. 431–444. DOI: https://doi.org/10.1016/j.stem.2014.03.009.

[36] Jeff W. M. Bulte et al. "Quantitative "Hot-Spot" Imaging of Transplanted Stem Cells Using Superparamagnetic Tracers and Magnetic Particle Imaging". In: *Tomography* 1.2 (2015), pp. 91–97. DOI: 10.18383/j.tom.2015.00172.

[37] Olivia C. Sehl et al. "Trimodal Cell Tracking In Vivo: Combining Iron- and Fluorine-Based Magnetic Resonance Imaging with Magnetic Particle Imaging to Monitor the Delivery of Mesenchymal Stem Cells and the Ensuing Inflammation". In: *Tomography* 5.4 (2019), pp. 367–376. DOI: 10.18383/j.tom.2019.00020.

[38] Yaojiong Wu and Robert C. H. Zhao. "The Role of Chemokines in Mesenchymal Stem Cell Homing to Myocardium". In: *Stem Cell Reviews and Reports* 8.1 (Mar. 2012), pp. 243–250. DOI: 10.1007/s12015-011-9293-z.

[39] Matthew T. Harting et al. "Intravenous mesenchymal stem cell therapy for traumatic brain injury". In: *Journal of neurosurgery* 110.6 (June 2009), pp. 1189–1197. DOI: 10.3171/2008.9.JNS08158.

[40] Dorota A. Kedziorek et al. "Gene expression profiling reveals early cellular responses to intracellular magnetic labeling with superparamagnetic iron oxide nanoparticles". In: *Magnetic Resonance in Medicine* 63.4 (2010), pp. 1031–1043. DOI: https://doi.org/10.1002/mrm.22290.

[41] Mick M. Welling et al. "In vivo biodistribution of stem cells using molecular nuclear medicine imaging". In: *Journal of Cellular Physiology* 226.6 (June 2011), pp. 1444–1452. ISSN: 0021-9541. DOI: 10.1002/jcp.22539.

[42] Geoffrey Michael Currie, Hosen Kiat, and Janelle M. Wheat. "Scintigraphic Evaluation of Acute Lower Gastrointestinal Hemorrhage: Current Status and Future Directions". In: *Journal of Clinical Gastroenterology* 45.2 (2011).

[43] Bruce Lee and Andrew Newberg. "Neuroimaging in traumatic brain imaging". In: *NeuroRX* 2.2 (Apr. 2005), pp. 372–383. ISSN: 1545-5343. DOI: 10.1602/neurorx.2.2.372.

[44] Ryan Orendorff et al. "Firstiin vivo/itraumatic brain injury imaging via magnetic particle imaging". In: *Physics in Medicine and Biology* 62.9 (Apr. 2017), pp. 3501–3509. DOI: 10.1088/1361-6560/aa52ad.

[45] Elaine Y. Yu et al. "Magnetic Particle Imaging for Highly Sensitive, Quantitative, and Safe in Vivo Gut Bleed Detection in a Murine Model". In: *ACS Nano* 11.12 (Dec. 2017), pp. 12067–12076. ISSN: 1936-0851. DOI: 10.1021/acsnano.7b04844.

[46] Ajay Kumar Gupta and Mona Gupta. "Synthesis and surface engineering of iron oxide nanoparticles for biomedical applications". In: *Biomaterials* 26.18 (2005), pp. 3995–4021. ISSN: 0142-9612. DOI: https://doi.org/10.1016/j.biomaterials.2004.10.012.

[47] Patryk Szwargulski et al. "Monitoring Intracranial Cerebral Hemorrhage Using Multicontrast Real-Time Magnetic Particle Imaging". In: *ACS Nano* 14.10 (Oct. 2020), pp. 13913–13923. DOI: 10.1021/acsnano.0c06326.

[48] Peter Reimer and Thomas Balzer. "Ferucarbotran (Resovist): a new clinically approved RES-specific contrast agent for contrast-enhanced MRI of the liver: properties, clinical development, and applications". In: *European Radiology* 13.6 (June 2003), pp. 1266–1276. ISSN: 1432-1084. DOI: 10.1007/s00330-002-1721-7.

[49] Paul Keselman et al. "Tracking short-term biodistribution and long-term clearance of SPIO tracers in magnetic particle imaging". In: *Physics in Medicine and Biology* 62.9 (Apr. 2017), pp. 3440–3453. DOI: 10.1088/1361-6560/aa5f48.

[50] S. L. Brown, J. W. Hunt, and R. P. Hill. "Differential thermal sensitivity of tumour and normal tissue microvascular response during hyperthermia". In: *International Journal of Hyperthermia* 8.4 (1992), pp. 501–514. DOI: 10.3109/02656739209037988.

[51] Shuming Nie. "Understanding and overcoming major barriers in cancer nanomedicine". In: *Nanomedicine (London, England)* 5.4 (June 2010), pp. 523–528. DOI: 10.2217/nnm.10.23.

[52] Zhi Wei Tay et al. "Magnetic Particle Imaging-Guided Heating in Vivo Using Gradient Fields for Arbitrary Localization of Magnetic Hyperthermia Therapy". In: *ACS nano* 12.4 (Apr. 2018), pp. 3699–3713. ISSN: 1936-086X. DOI: 10.1021/acsnano.8b00893.

[53] Carmen Kut et al. "Preliminary study of injury from heating systemically delivered, nontargeted dextran-superparamagnetic iron oxide nanoparticles in mice". In: *Nanomedicine (London, England)* 7.11 (Nov. 2012), pp. 1697–1711. DOI: 10.2217/nnm.12.65.

[54] Lisa M. Bauer et al. "High-performance iron oxide nanoparticles for magnetic particle imaging – guided hyperthermia (hMPI)". In: *Nanoscale* 8 (24 2016), pp. 12162–12169. DOI: 10.1039/C6NR01877G.

[55] Daniel Hensley et al. "Combining magnetic particle imaging and magnetic fluid hyperthermia in a theranostic platform". In: *Physics in Medicine and Biology* 62 (Apr. 2017), p. 3483. DOI: 10.1088/1361-6560/aa5601.

[56] M I Shliomis. "Magnetic fluids". In: *Soviet Physics Uspekhi* 17.2 (Feb. 1974), pp. 153–169. DOI: 10.1070/pu1974v017n02abeh004332.

[57] Patrick W. Goodwill and Steven M. Conolly. "The X-Space Formulation of the Magnetic Particle Imaging Process: 1-D Signal, Resolution, Bandwidth, SNR, SAR, and Magnetostimulation". In: *IEEE Transactions on Medical Imaging* 29.11 (2010), pp. 1851–1859. DOI: 10.1109/TMI.2010.2052284.

[58] Laura R. Croft, Patrick W. Goodwill, and Steven M. Conolly. "Relaxation in x-space magnetic particle imaging". In: *IEEE transactions on medical imaging* 31.12 (Dec. 2012), pp. 2335–2342. ISSN: 1558-254X. DOI: 10.1109/TMI.2012.2217979.

[59] Louis Néel. "Théorie du traînage magnétique des ferromagnétiques en grains fins avec application aux terres cuites," in: *Annals of Geophysics* 5 (1949), pp. 99–136.

[60] R. E. Rosensweig. "Heating magnetic fluid with alternating magnetic field". In: *Journal of Magnetism and Magnetic Materials* 252 (Nov. 2002), pp. 370–374. ISSN: 0304-8853.

[61] Sophie Laurent et al. "Magnetic Iron Oxide Nanoparticles: Synthesis, Stabilization, Vectorization, Physicochemical Characterizations, and Biological Applications". In: *Chemical Reviews* 108.6 (June 2008), pp. 2064–2110. ISSN: 0009-2665. DOI: 10.1021/cr068445e.

[62] Volkmar Weissig, Tracy K. Pettinger, and Nicole Murdock. "Nanopharmaceuticals (part 1): products on the market". In: *International journal of nanomedicine* 9 (Sept. 2014), pp. 4357–4373. ISSN: 1178-2013. DOI: 10.2147/IJN.S46900.

[63] Hossein Nejadnik et al. "Ferumoxytol Can Be Used for Quantitative Magnetic Particle Imaging of Transplanted Stem Cells". In: *Molecular imaging and biology* 21.3 (June 2019), pp. 465–472. ISSN: 1860-2002. DOI: 10.1007/s11307-018-1276-x.

[64] Zhi Wei Tay et al. "The Relaxation Wall: Experimental Limits to Improving MPI Spatial Resolution by Increasing Nanoparticle Core size". In: *Biomedical physics & engineering express* 3.3 (June 2017), p. 035003. DOI: 10.1088/2057-1976/aa6ab6.

[65] L. R. Croft et al. "Low drive field amplitude for improved image resolution in magnetic particle imaging". In: *Med Phys* 43.1 (Jan. 2016), p. 424.

[66] Z. W. Tay et al. "Pulsed Excitation in Magnetic Particle Imaging". In: *IEEE Trans Med Imaging* 38.10 (Oct. 2019), pp. 2389–2399.

[67] Zhi Wei Tay et al. "Optimization of Drive Parameters for Resolution, Sensitivity and Safety in Magnetic Particle Imaging". In: *IEEE Transactions on Medical Imaging* 39.5 (2020), pp. 1724–1734. DOI: 10.1109/TMI.2019.2957041.

[68] C. Kuhlmann et al. "Drive-field Frequency Dependent MPI Performance of Single-Core Magnetite Nanoparticle Tracers". In: *IEEE Trans Magn* 51.2 (Feb. 2015).

[69] Erica E. Mason et al. "Design analysis of an MPI human functional brain scanner". eng. In: *International journal on magnetic particle imaging* 3.1 (2017), p. 1703008.

[70] Prashant Chandrasekharan et al. "A perspective on a rapid and radiation-free tracer imaging modality, magnetic particle imaging, with promise for clinical translation". In: *The British Journal of Radiology* 91.1091 (2018), p. 20180326. DOI: 10.1259/bjr.20180326.

[71] D Pouliquen et al. "Superparamagnetic iron oxide nanoparticles as a liver MRI contrast agent: Contribution of microencapsulation to improved biodistribution". In: *Magnetic Resonance Imaging* 7.6 (1989), pp. 619–627. ISSN: 0730-725X. DOI: https://doi.org/10.1016/0730-725X(89)90530-4.

[72] Y. Gandon et al. "[Super-paramagnetic iron oxide: an MRI contrast media for the reticuloendothelial system]". In: *Ann Radiol (Paris)* 32.4 (1989), pp. 267–272.

[73] Heike E. Daldrup-Link et al. "MRI of Tumor-Associated Macrophages with Clinically Applicable Iron Oxide Nanoparticles". In: *Clinical Cancer Research* 17.17 (Sept. 2011), pp. 5695–5704. ISSN: 1078-0432. DOI: 10.1158/1078-0432.CCR-10-3420.

[74] V. S. Balakrishnan et al. "Physicochemical properties of ferumoxytol, a new intravenous iron preparation". In: *European Journal of Clinical Investigation* 39.6 (2009), pp. 489–496. DOI: https://doi.org/10.1111/j.1365-2362.2009.02130.x.

[75] Maureen N. Hood, Anne Dorte Blankholm, and Alan Stolpen. "The Rise of Off-Label Iron-Based Agents in Magnetic Resonance Imaging". In: *Journal of Radiology Nursing* 38.1 (2019), pp. 38–41. ISSN: 1546-0843. DOI: https://doi.org/10.1016/j.jradnu.2018.11.004.

[76] Mustafa R. Bashir et al. "Emerging applications for ferumoxytol as a contrast agent in MRI". In: *Journal of Magnetic Resonance Imaging* 41.4 (2015), pp. 884–898. DOI: https://doi.org/10.1002/jmri.24691.

[77] Food and Drug Administration. *FDA Drug Safety Communication: FDA strengthens warnings and changes prescribing instructions to decrease the risk of serious allergic reactions with anemia drug Feraheme (ferumoxytol).* 2016. URL: https://www.fda.gov/media/91415/download.

[78] George R. Bailie. "Comparison of rates of reported adverse events associated with i.v. iron products in the United States". In: *American Journal of Health-System Pharmacy* 69.4 (Feb. 2012), pp. 310–320. DOI: 10.2146/ajhp110262.

[79] Shreyas S. Vasanawala et al. "Safety and technique of ferumoxytol administration for MRI". In: *Magnetic Resonance in Medicine* 75.5 (2016), pp. 2107–2111. DOI: https://doi.org/10.1002/mrm.26151.

[80] Erika C. Vreeland et al. "Enhanced Nanoparticle Size Control by Extending LaMer's Mechanism". In: *Chemistry of Materials* 27.17 (Sept. 2015), pp. 6059–6066. ISSN: 0897-4756. DOI: 10.1021/acs.chemmater.5b02510.

[81] Victor K. LaMer and Robert H. Dinegar. "Theory, Production and Mechanism of Formation of Monodispersed Hydrosols". In: *Journal of the American Chemical Society* 72.11 (Nov. 1950), pp. 4847–4854. ISSN: 0002-7863. DOI: 10.1021/ja01167a001.

[82] Nguyen T. K. Thanh, N. Maclean, and S. Mahiddine. "Mechanisms of Nucleation and Growth of Nanoparticles in Solution". In: *Chemical Reviews* 114.15 (Aug. 2014), pp. 7610–7630. ISSN: 0009-2665. DOI: 10.1021/cr400544s.

[83] Tadao Sugimoto. "Preparation of monodispersed colloidal particles". In: *Advances in Colloid and Interface Science* 28 (Jan. 1987), pp. 65–108.

[84] Wei Wu, Quanguo He, and Changzhong Jiang. "Magnetic Iron Oxide Nanoparticles: Synthesis and Surface Functionalization Strategies". In: *Nanoscale Research Letters* 3.11 (Oct. 2008), p. 397. ISSN: 1556-276X. DOI: 10.1007/s11671-008-9174-9.

[85] Amit P. Khandhar et al. "Monodisperse magnetite nanoparticle tracers for in vivo magnetic particle imaging". In: *Biomaterials* 34.15 (May 2013), pp. 3837–3845. ISSN: 0142-9612.

[86] R. Matthew Ferguson, Amit P. Khandhar, and Kannan M. Krishnan. "Tracer design for magnetic particle imaging (invited)". In: *Journal of Applied Physics* 111.7 (Apr. 2012), 07B318. ISSN: 0021-8979. DOI: 10.1063/1.3676053.

[87] R. Matthew Ferguson, Kevin R. Minard, and Kannan M. Krishnan. "Optimization of nanoparticle core size for magnetic particle imaging". In: *Journal of Magnetism and Magnetic Materials* 321.10 (May 2009), pp. 1548–1551. ISSN: 0304-8853.

[88] Bo Chen et al. "An efficient synthesis of ferumoxytol induced by alternating-current magnetic field". In: *Materials Letters* 170 (2016), pp. 93–96. ISSN: 0167-577X. DOI: https://doi.org/10.1016/j.matlet.2016.02.006.

[89] Nene Ajinkya et al. "Magnetic Iron Oxide Nanoparticle (IONP) Synthesis to Applications: Present and Future". In: *Materials* 13.20 (2020). ISSN: 1996-1944. DOI: 10.3390/ma13204644.

[90] Nikhil R. Jana, Yongfen Chen, and Xiaogang Peng. "Size- and Shape-Controlled Magnetic (Cr, Mn, Fe, Co, Ni) Oxide Nanocrystals via a Simple and General Approach". In: *Chemistry of Materials* 16.20 (Oct. 2004), pp. 3931–3935. DOI: 10.1021/cm049221k.

[91] M Graeser, K Bente, and T M Buzug. "Dynamic single-domain particle model for magnetite particles with combined crystalline and shape anisotropy". In: *Journal of Physics D: Applied Physics* 48.27 (June 2015).

[92] Zhi Wei Tay et al. "A High-Throughput, Arbitrary-Waveform, MPI Spectrometer and Relaxometer for Comprehensive Magnetic Particle Optimization and Characterization". In: *Scientific reports* 6 (Sept. 2016), pp. 34180–34180. ISSN: 2045-2322. DOI: 10.1038/srep34180.

[93] P. W. Goodwill et al. "An x-space magnetic particle imaging scanner". In: *Rev Sci Instrum* 83.3 (Mar. 2012), p. 033708.

[94] P. W. Goodwill et al. "Ferrohydrodynamic relaxometry for magnetic particle imaging". In: *Applied Physics Letters* 98.26 (2011), p. 262502. DOI: 10.1063/1.3604009.

[95] Matthias Graeser et al. "Analog receive signal processing for magnetic particle imaging". In: *Medical Physics* 40.4 (2013), p. 042303.

[96] André Behrends, Matthias Graeser, and Thorsten M. Buzug. "Introducing a frequency-tunable magnetic particle spectrometer". In: *Current Directions in Biomedical Engineering* 1.1 (2015), pp. 249–253. DOI: doi:10.1515/cdbme-2015-0062.

[97] Saqlain A. Shah, R. M. Ferguson, and K. M. Krishnan. "Slew-rate dependence of tracer magnetization response in magnetic particle imaging". In: *Journal of Applied Physics* 116.16 (2014), p. 163910. DOI: 10.1063/1.4900605.

[98] Asahi Tomitaka et al. "Variation of Magnetic Particle Imaging Tracer Performance With Amplitude and Frequency of the Applied Magnetic Field". In: *IEEE Transactions on Magnetics* 51.2 (2015), pp. 1–4. DOI: 10.1109/TMAG.2014.2341570.

[99] Zhi Wei Tay. "Novel Scanning Strategies in x-Space Magnetic Particle Imaging for Improved Imaging Performance and Theranostic Applications". In: *UC Berkeley* (). ProQuest ID: Tay$_b erkeley_0 028E_1 7752$.

[100] Xinyi Y. Zhou et al. "First in vivo magnetic particle imaging of lung perfusion in rats". In: *Physics in medicine and biology* 62.9 (May 2017), pp. 3510–3522. ISSN: 1361-6560. DOI: 10.1088/1361-6560/aa616c.

[101] Peter Ludewig et al. "Magnetic particle imaging for assessment of cerebral perfusion and ischemia". In: *WIREs Nanomedicine and Nanobiotechnology* 14.1 (2022), e1757. DOI: https://doi.org/10.1002/wnan.1757.

[102] Peter Ludewig et al. "Magnetic Particle Imaging for Real-Time Perfusion Imaging in Acute Stroke". In: *ACS Nano* 11.10 (Oct. 2017), pp. 10480–10488. ISSN: 1936-0851. DOI: 10.1021/acsnano.7b05784.

[103] I. Molwitz et al. "First magnetic particle imaging angiography in human-sized organs by employing a multimodal ex vivo pig kidney perfusion system". In: *Physiol Meas* 40.10 (Oct. 2019), p. 105002.

[104] Angelie Rivera-Rodriguez et al. "Tracking adoptive T cell immunotherapy using magnetic particle imaging". In: *Nanotheranostics* 5.4 (Apr. 2021), pp. 431–444. DOI: 10.7150/ntno.55165.

[105] N. Panagiotopoulos et al. "Magnetic particle imaging: current developments and future directions". In: *Int J Nanomedicine* 10 (2015), pp. 3097–3114.

[106] M. Graeser et al. "Human-sized magnetic particle imaging for brain applications". In: *Nature Communications* 10.1 (Apr. 2019), p. 1936. ISSN: 2041-1723. DOI: 10.1038/s41467-019-09704-x.

[107] Jürgen Rahmer et al. "Signal encoding in magnetic particle imaging: properties of the system function". In: *BMC Medical Imaging* 9.1 (Apr. 2009), p. 4. ISSN: 1471-2342. DOI: 10.1186/1471-2342-9-4.

[108] Ryan Hufschmid et al. "Synthesis of phase-pure and monodisperse iron oxide nanoparticles by thermal decomposition". In: *Nanoscale* 7 (25 2015), pp. 11142–11154. DOI: 10.1039/C5NR01651G.

[109] Zhi Wei Tay et al. "Superferromagnetic Nanoparticles Enable Order-of-Magnitude Resolution & Sensitivity Gain in Magnetic Particle Imaging". In: *Small Methods* 5.11 (2021), p. 2100796. DOI: https://doi.org/10.1002/smtd.202100796.

[110] Denis G. Rancourt. "Magnetism of Earth, Planetary, and Environmental Nanomaterials". In: *Reviews in Mineralogy and Geochemistry* 44.1 (Jan. 2001), pp. 217–292. ISSN: 1529-6466. DOI: 10.2138/rmg.2001.44.07.

[111] A. Zeleňáková et al. "Superferromagnetism in chain-like Fe@SiO2 nanoparticle ensembles". In: *Journal of Applied Physics* 116.3 (2014), p. 033907. DOI: 10.1063/1.4890354.

[112] A. A. Timopheev et al. "Coercivity anomaly in the superferromagnetic state of an ensemble of nanoparticles with oriented anisotropy". In: *Journal of Applied Physics* 108.5 (2010), p. 053902. DOI: 10.1063/1.3480802.

[113] P. A. Valberg and J. P. Butler. "Magnetic particle motions within living cells. Physical theory and techniques". In: *Biophysical journal* 52.4 (Oct. 1987), pp. 537–550. ISSN: 0006-3495. DOI: 10.1016/S0006-3495(87)83243-5.

[114] Sébastien Boutry et al. "How to quantify iron in an aqueous or biological matrix: a technical note". In: *Contrast Media & Molecular Imaging* 4.6 (), pp. 299–304. DOI: https://doi.org/10.1002/cmmi.291.

[115] N. Tripathi. "Densities, Viscosities, and Refractive Indices of Mixtures of Hexane with Cyclohexane, Decane, Hexadecane, and Squalane at 298.15 K". In: *International Journal of Thermophysics* 26.3 (May 2005), pp. 693–703. ISSN: 1572-9567. DOI: 10.1007/s10765-005-5572-8.

[116] John David Jackson. *Classical electrodynamics*. 3rd ed. New York, NY: Wiley, 1999. ISBN: 9780471309321.

[117] 1939- Taylor John R. (John Robert). *Classical mechanics*. Sausalito, Calif. : University Science Books, [2005] ©2005, [2005].

[118] Jos van Rijssel, Bonny W.M. Kuipers, and Ben H. Erné. "Bimodal distribution of the magnetic dipole moment in nanoparticles with a monomodal distribution of the physical size". In: *Journal of Magnetism and Magnetic Materials* 380 (2015), pp. 325–329. ISSN: 0304-8853. DOI: https://doi.org/10.1016/j.jmmm.2014.09.058.

[119] J. T. Finer, R. M. Simmons, and J. A. Spudich. "Single myosin molecule mechanics: piconewton forces and nanometre steps". In: *Nature* 368.6467 (Mar. 1994), pp. 113–119.

[120] K. L. Barry Fung. "Elucidating super-resolution Magnetic Particle Imaging: superferromagnetic remanence decay through MPI signal evolution informs super-resolution MPI scan strategies". In: *Proceedings of the World Molecular Imaging Congress 2021, October 5-8, 2021: Late-Breaking Abstracts* 23.2 (Dec. 2021), pp. 1739–2027. ISSN: 1860-2002. DOI: 10.1007/s11307-021-01694-x.

[121] Moritz F. Kircher, Sanjiv S. Gambhir, and Jan Grimm. "Noninvasive cell-tracking methods". In: *Nature Reviews Clinical Oncology* 8.11 (Nov. 2011), pp. 677–688. ISSN: 1759-4782. DOI: 10.1038/nrclinonc.2011.141.

[122] Steven A. Rosenberg and Nicholas P. Restifo. "Adoptive cell transfer as personalized immunotherapy for human cancer". In: *Science* 348.6230 (2015), pp. 62–68. DOI: 10.1126/science.aaa4967.

[123] Rinat Meir et al. "Nanomedicine for Cancer Immunotherapy: Tracking Cancer-Specific T-Cells in Vivo with Gold Nanoparticles and CT Imaging". In: *ACS Nano* 9.6 (June 2015), pp. 6363–6372.

[124] Andrew Micieli et al. "Chapter 5 - Stroke imaging: Noncontrast head CT". In: *The Code Stroke Handbook*. Academic Press, Jan. 2020, pp. 107–132.

[125] Andrew Micieli et al. "Chapter 6 - Stroke imaging: CT angiography". In: *The Code Stroke Handbook*. Academic Press, Jan. 2020, pp. 133–150. ISBN: 978-0-12-820522-8.

[126] Andrew Micieli et al. "Chapter 7 - Stroke imaging: CT perfusion". In: *The Code Stroke Handbook*. Academic Press, Jan. 2020, pp. 151–163.

[127] Clarissa Zimmerman Cooley et al. "Rodent Cerebral Blood Volume (CBV) changes during hypercapnia observed using Magnetic Particle Imaging (MPI) detection". In: *NeuroImage* 178 (Sept. 2018), pp. 713–720. ISSN: 1095-9572. DOI: 10.1016/j.neuroimage.2018.05.004.